Modeling of Dislocation Interaction with Solutes, Nano-Precipitates and Interfaces: A Multiscale Challenge

Nicholas G. Kioussis[1, *] and Nasr M. Ghoniem[2]

[1] *Department of Physics, California State University Northridge, Northridge, CA 91330-8268, USA*
[2] *Mechanical and Aerospace Engineering Department, University of California Los Angeles, CA 90095-1597, USA*

We review here several multiscale methods that we have developed to determine dislocation properties and interactions in metals. The review includes: (1) dislocation core properties in fcc and bcc metals; (2) the effect of solutes or nanoprecipitates on the mobility of a screw dislocation in bcc metals; (3) the interaction between dislocations and precipitates in intermetallic compounds; and (4) the transmission of dislocations through coherent and incoherent interfaces. In the concurrent quantum mechanical (QM) and molecular mechanical (MM) coupling approach, the quantum mechanical treatment is spatially confined to a small region, surrounded by a larger classical atomistic region. This approach is particularly useful for systems where quantum mechanical interactions in a small region, such as lattice defects or chemical impurities, can affect the macroscopic properties of a material. We discuss how the coupling across the different scales can be accomplished efficiently and accurately. We have applied this method to study the core structure and mobility of an edge dislocation in Al and of a screw dislocation in Ta, which are prototypical fcc and bcc metals. We find that the *local environment* of W solutes in Ta has a dramatic effect both on the dislocation mobility and slip paths. Isolated W solutes enhance the dislocation mobility, W nanoclusters of triangular shape pin the dislocation, while those of hexagonal shape result in spontaneous dislocation glide. The first sequential multiscale approach is a hybrid *ab initio*-based approach of Suzuki's atomic-row (AR) model, which allows the study of the dislocation core of a screw dislocation in bcc metals. The second hybrid approach, based on an extension of the Peierls-Nabarro model to study the dislocation-interface and the dislocation-precipitate interactions, integrates the atomistic nature from *ab initio* calculations of the generalized stacking fault energy surface (GSFS) into the parametric dislocation dynamics method. The *ab initio*-based calculations reveal that Cu nano-clusters in α-Fe dramatically alter the core structure of a screw dislocation from non-polarized in pure Fe to polarized, in agreement with experiments. In contrast, Cr clusters do not change the core polarization and increase the Peierls stress, thus hardening Fe. The hybrid method with four different interaction models was applied to study the interaction of a superdislocation with a spherical γ-precipitate embedded in the γ'-matrix of a nickel-based superalloy. The dislocation core structure was found to play an important role in determining the critical resolved shear stress. Based on these simulations, analytical equations for the precipitate strengthening are derived. For the Cu/Ni interface, the dislocation is found to dissociate into partials in both Cu and Ni, and the dislocation core is squeezed near the interface facilitating the spreading process, and leaving an interfacial ledge. It is shown that the strength of the bimaterial can be greatly enhanced by the spreading of the glide dislocation, and also increased by the pre-existence of misfit dislocations.

Keywords:

CONTENTS

*Author to whom correspondence should be addressed.

1. INTRODUCTION

Dislocations, which are one-dimensional topological defects, are central to the understanding of mechanical properties of metals. The creation and motion of dislocations mediate the plastic response of a crystal to external stress. While the continuum elasticity theory describes well the long-range elastic strain of a dislocation for length scales beyond a few lattice spacings, it breaks down near the singularity in the region surrounding the dislocation center, known as the dislocation core. The discrete nature of the crystalline lattice avoids the conceptual difficulty posed by the continuum singularity and recovers the structural differentiation smoothed out by the continuum elasticity. There has been a great deal of interest in describing accurately the dislocation core structure on an atomic scale because of its important role in many phenomena of crystal plasticity. The core properties control, for instance, the mobility of dislocations, which accounts for the intrinsic ductility or brittleness of solids. The core is also important for the interaction of dislocations at close distances, which are relevant to plastic deformation. The atomic positions around the dislocation core can be studied experimentally by, e.g., transmission- or high-resolution electron microscopes.[1–4]

Face-centered cubic (fcc) and body-centered cubic (bcc) metals and their alloys exhibit unique mechanical properties that make them attractive both for structural applications at elevated temperatures and for interconnect applications. An inherent drawback limiting the use of bcc materials as structural components is their reduced low-temperature toughness, which in turn increases the propensity towards fracture. Thus, the challenge in design of advanced alloys is to combine strengthening and

Nicholas G. Kioussis finished his undergraduate studies in Physics at the University Athens, Greece, and then obtained M.S and Ph.D. degrees in Theoretical Condensed Matter Physics from the University of Illinois at Chicago in 1984. He was appointed an assistant Professor at CSUN in 1987. He became a full professor in 2003, and was promoted to the rank of GRIF professor in 2009. His research interests cover a wide spectrum of diverse areas from fundamental research to applied problems in theoretical condensed matter physics and materials science. These range from first principles electronic structure, phenomenological Anderson Hamiltonians, and hybrid of such methods, for studies of strongly-correlated electron systems; multiscale modeling of mechanical properties of metals and intermetallics; multiscale modeling of defects (point defects, dislocations and voids) under irradiation; *ab initio* calculations of the electronic, magnetic, mechanical, and optical properties of materials; and studies of spin transport in magnetic tunnel barriers, quantum dots, and in DNA. Kioussis founded and continues to be director of the W. M. Keck Computational Materials Theory Science Center (CMTC) at CSUN. He has received the outstanding faculty award in 2009, the Marie Curie International Incoming Fellowship in 2008, the Donald Bianchi Award for Research Excellence in 2004, the Department of Energy Faculty Fellowship during 1988–1990, and was elected a Kavli Scholar at UC Santa Barbara in 2005. He is a member of APS, TMS, and MRS. He has published over 110 peer reviewed articles, has edited three books, and has organized four international conferences.

Nasr M. Ghoniem finished his undergraduate studies in Nuclear Engineering at the University of Alexandria, and then obtained an M.Eng. Degree in Engineering Physics (Solid State) from McMaster University in Canada, and MS and Ph.D. degrees in Nuclear Engineering (Nuclear Materials) from the University of Wisconsin (USA) in 1977. He was appointed an assistant Professor at UCLA in 1977. He became a full professor in 1986, and was promoted to the senior rank in the UC system in 1996 and to the rank of distinguished professor (above scale) in 2006. His research interests are in the areas of damage and failure of materials in mechanical and nuclear design; mechanics and physics of material defects (point defects, dislocations, voids and cracks); material degradation in severe environments (e.g., nuclear, fusion energy, rocket engines, etc.); plasma and laser processing of materials; non-equilibrium, pattern formation and instability phenomena; and radiation interaction with materials (neutrons, electrons, particles, laser and photons). Ghoniem was elected fellow of the American Nuclear Society in 1994, and is a member of ANS, TMS, MRS, APS, and AAM. He was awarded the Outstanding Young Man of America Award in 1978, the ANS Lifetime Outstanding Achievement Award in 1998, fellowship of the Japan Society for the Promotion of Sciences (JSPS) in 1998, and was granted the Royal Society of London Visiting Professorship in Hong Kong in 1999. As a result of his research on the plasticity and failure of materials in irradiated and high-temperature materials, he was elected fellow of ASME in 2006.

REVIEW

toughening phases with a better balance of properties. The dislocation core behavior in fcc and bcc materials is very different.

The core in fcc tends to be planar and is associated with the sliding of the close-packed (111) crystal planes across one another. A full dislocation with burgers vector $\mathbf{b} = a/D2\langle 110 \rangle$ (in units of the lattice parameter a) dissociates into two Shockley partial dislocations, bounding an area of stacking fault (SF) according to the scheme,

$$\mathbf{b} \rightarrow \mathbf{b_{1p}} + \mathbf{b_{2p}}$$

$$\frac{a}{2}[110] \rightarrow \frac{a}{6}[21\bar{1}] + SF + \frac{a}{6}[121] \qquad (1)$$
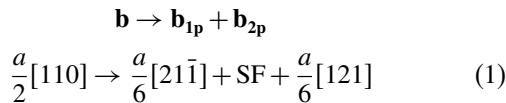
Because the partial Burgers vectors lie on the same (111) plane, the Shockley partials glide in that plane and spread out in extent. The presence of SF in fcc metals stems from the particular ABCABCABC sequence of (111) planes. The equilibrium splitting width, d, of the dissociated dislocation is determined by the balance of the repulsive elastic forces and the attractive force from the stacking faults. For example, for the perfect edge dislocation, continuum elastic theory gives a partials separation of

$$d_{SF} = \frac{\mu b^2}{24\pi\gamma_{isf}} \frac{2+\nu}{1-\nu} \qquad (2)$$

where $b = a/\sqrt{2}$ is the Burgers vector, ν is the Poisson's ratio, and γ_{isf} is the intrinsic stacking fault energy. The intrinsic stacking-fault configuration corresponds to a slip of $b_p = a/\sqrt{6}$ in the Ref. [112] direction, resulting in the stacking ABC|BCABC. Values of stacking fault energies in fcc metals lie in the range of 30 mJ/m^2 (Ag) to 170 mJ/m^2 (Al), except for the anomalous high value of 400 mJ/m^2 in Ir.[5] The value of d serves as a check of the reliability of the multiscale method employed.

The microscopic origin of plasticity is far more complex and less well understood in bcc metals than in their fcc counterparts. In bcc metals stable stacking faults do not exist and the plastic deformation is mainly controlled by the intrinsic core properties of $a/2\langle 111 \rangle$ screw dislocations. Unlike the highly mobile edge dislocations, the motion of screw dislocations is restricted by a non-planar atomic core structure which must contract before it moves. The most prominent aspects of the deformation behavior of bcc materials that relate to properties of screw dislocations are the characteristic temperature (for $T < 0.2T_{melt}$, where T_{melt} is the melting temperature) and strain-rate dependence of the flow stress, the twinning-antitwinning asymmetry of the yield and flow stresses, and the existence of a ductile-to-brittle transition at low temperature.[6, 7] At very low temperatures or at extreme strain rates the screw dislocations move as straight lines, while at finite temperatures and usual strain rates their motion proceeds via formation and migration of pairs of kinks.[6]

However, in most situations, dislocation behavior is considerably different in the realistically *dirty* materials, where dislocation mobility can vary by several orders of magnitude, depending on the type, concentration, and local environment of the solute. Since plastic deformation in metals is mediated by the motion dislocations that produce a long-range stress, the dislocation-solute or dislocation-precipitate interaction is of great practical importance. Solute atoms or nano-clusters, which are ubiquitous in metals, play a key role in altering their mechanical properties (e.g., strength, ductility). Experimental studies during the past several decades indicate that solutes can give rise to both solid-solution hardening (SSH) and softening (SSS).[8, 9] In the SSS phenomenon, the effect of alloying decreases the yield strength at low temperatures and low impurity concentrations. These observations clearly suggest that another contribution to dislocation mobility stems from a rather strong sensitivity to trace amounts of substitutional and/or interstitial impurities, the origin of which has not yet been clarified.[10] The intrinsic mechanisms of SSS have been attributed to mismatch in size and in shear moduli between solute and matrix atoms. However, recently, the *chemical* or *electronic* mechanism on both the kink formation and migration rates in Mo has been shown to play an important role.[11, 12] An outstanding challenge for dislocation modeling is an accurate and realistic description of interactions between dislocations and impurity atoms and clusters. Such a description can provide the basis for understanding the thermodynamics and kinetics of co-evolution of dislocation and alloy microstructures.

The influence of interfaces on the mechanical properties of multiphase and polycrystalline materials is ubiquitous.[13] Interfaces serve as barriers to dislocation motion modifying the strength, as easy paths for crack propagation affecting toughness, etc. Nanolayered metallic composites, composed of alternating layers of soft metals, have been shown[14] to possess strengths of several GPa, often within a factor of two to three of the theoretical strength limit, when the bilayer periods are on the order of a few nanometers. Experiments on model systems such as Cu–Ni[15] and Cu–Nb[16] indicate that, in the micron to sub-micron range, the strengths of these materials increase with microstructural refinement according to the Hall-Petch relation[17, 18]

$$\tau_{HP} = \tau_0 + \frac{k_{HP}}{\sqrt{d}} \qquad (3)$$

where τ_{HP} is the critical resolved shear stress required to push the leading dislocation in the pile-up past the obstacle, τ_0 is a friction stress for dislocation glide, d is the distance between the barriers, $k_{HP} = \sqrt{\mu b \tau_{cr}/\pi}$ is the Hall-Petch coefficient, and μ is the shear modulus. However, as the layer thickness is reduced to the nm-scale, the number of dislocations in a pile-up approaches unity and the pile-up based Hall-Petch model ceases to apply. In the few to a few tens of nanometers range, the increase in yield strength of nanolaminates with decreasing layer thickness is interpreted in terms of the confined layer slip

of single dislocations. As layer thickness is decreased to a couple nanometers, the strength reaches a peak with weak or no dependence on layer thickness. It has been suggested that the peak strength is determined by the stress needed to transmit single dislocations across the interface.[19]

Studies of large atomic systems require approximations and simplifications when describing atomic interactions that may, however, obliterate some important features of bonding. For this reason, the most challenging aspect of materials modeling is the choice of the description of atomic interactions that correctly and with sufficient accuracy reflects the physics of bonding in any specific case, while at the same time it is computationally tractable. In Section 2, we review various concurrent and sequential multiscale approaches we have developed recently, to study the dislocation core properties in
(1) fcc and bcc metals;
(2) the effect of chemistry on the dislocation mobility; and
(3) the transmission of a dislocation through a coherent and incoherent interface.

In Section 3.1 we present results for the dislocation core properties, including the Peierls stress for an edge dislocation in Al using the improved concurrent multiscale method. In Section 3.2 we present results of the concurrent multiscale approach of the effect of the local environment (random solid solution or nano-clusters of different geometry) of W in Ta on the dislocation mobility. In Section 3.3 we employ the sequential inter-row multiscale approach to study the effect of Cu or Cr solutes and solute-clusters on the dislocation core properties of the $a/2\langle 111 \rangle$ screw dislocation in α-Fe. The hybrid atomistic-continuum approach is presented in Section 3.4 to study the interaction between a superdislocation and γ-precipitates embedded in the γ' matrix of a nickel-based superalloy. In Section 3.5 we present results for the transmission of a dislocation across a coherent and incoherent Cu–Ni interface. Finally, we present our conclusions in Section 4.

2. MULTISCALE APPROACHES

The challenge in computational materials science and engineering is that real materials usually exhibit phenomena on one scale that require a very accurate and computationally expensive description, and phenomena on another scale for which a coarser description is satisfactory and, in fact, necessary to avoid prohibitively large computations. It is the hope that multiscale modeling approaches may be the answer to such challenge. These computational approaches take advantage of the multiple scales present in a material and build unified descriptions by linking the models specialized at different scales.

There are two categories of multiscale simulations: sequential, consisting of passing information across scales, and concurrent, consisting of seamless coupling of scales.[20] The majority of multiscale simulations that are

currently in use are sequential, and are effective in systems where the various scales are weakly coupled. An example of a sequential approach is the Peierls-Nabarro (PN) model which essentially establishes a connection between atomic and continuum length scales.[21–23] The information passed across the scales is the generalized stacking fault energy surface which can be determined accurately from density functional theory (DFT) calculations. In systems where the coupling across different length scales is strong, concurrent approaches are usually required. In contrast to sequential approaches, concurrent simulations are still relatively new and only a few models have been developed to date.[24–39] In a concurrent simulation, the system is often partitioned into domains characterized by different scales and physics. The challenge of any concurrent approach lies in establishing a high quality coupling between the regions which are treated by different computational methods. Notably, Choly et al. have recently put forward a general concurrent method which couples DFT-based quantum mechanical (QM) simulations to classical molecular mechanics (MM) simulations for metallic materials.[30] The efficiency and accuracy of this coupling scheme have been demonstrated in bulk and a screw dislocation in Al. More recently, a multiscale approach was developed that concurrently couples DFT calculations for electrons, to the embedded-atom-method (EAM)[40] simulations for classical atoms, and to the finite-element modeling for elastic continuum in a unified fashion.[32] The approach, referred to as QCDFT is based on the formalism of Choly et al. and the quasicontinuum method [24, 29] and has been applied to study an edge dislocation in Al in the absence and presence of hydrogen impurities.[32] Despite the apparent success of the concurrent approach of Choly et al., non-negligible errors nonetheless exist across the DFT/EAM boundary.[30] More specifically, when the interaction energy between the quantum and classical regions is determined from a classical simulation, the forces on the atoms are determined by DFT and EAM *cluster* calculations where the fictitious surface effects cannot be fully canceled owing to the mismatch in DFT/EAM forces on the surface atoms. The surface effects can introduce substantial errors on the position of the atoms at the domain boundary, and degrade the coupling across the boundary.

In Section 2.1 we present an improvement over Choly's approach, which significantly reduces the coupling errors of the original approach.[38] We demonstrate the effectiveness of the improved approach by carrying out a comparative study of bulk Al. In Section 2.2 we describe two different sequential multiscale methods.

2.1. Concurrent Multiscale Approach

The concurrent multiscale approach is based on that proposed by Choly et al.,[30] which, however, significantly reduces the coupling error of the original approach.

The improved method does not introduce any additional computational effort and is easy to implement.[38, 39] Furthermore, it yields a Peierls stress for an edge dislocation in Al in good agreement with experiment and for Ta in excellent agreement with the FP-GFBC method,[37] which correctly couples the strain field of the dislocation core to the long-range elastic field. The system, shown in Figure 1, is divided into: Region I, which includes the dislocation core and the solutes, is treated within the framework of DFT; Region II which refers to the rest of the system is treated with the EAM or Finnis-Sinclair (FS) potentials; and the boundary (**B**) region, which is introduced to reduce the coupling errors between the two regions.

The total energy of the entire system can be expressed as[30]

$$E[I+II] = E_{DFT}[I] + E_{EAM}[II] + E^{int}[I, II] \quad (4)$$

Here, $E_{DFT}[I]$ is the energy of region I in the *absence* of region II obtained by DFT cluster calculations; $E_{EAM}[II]$ is the energy of region II obtained from EAM calculations in the absence of region I (i.e., void calculations); and $E^{int}[I, II]$ represents a formal interaction energy added to give the correct total energy of the entire system. The crux of multiscale modeling lies in the determination of $E^{int}[I, II]$. Different choices made for the calculation of $E^{int}[I, II]$ may result in distinct coupling methods. Similar energy expression of Eq. (4) had been proposed by others.[41]

The interaction energy between the subsystems I and II can be written formally as

$$E^{int}[I, II] \equiv E[I+II] - E[I] - E[II] \quad (5)$$
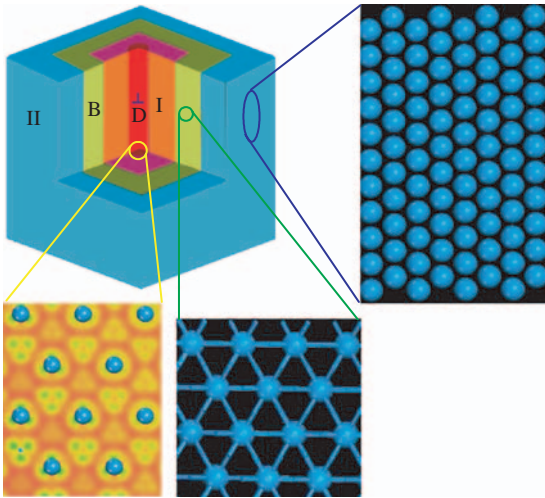
Fig. 1. Schematic view of the partitioned multiscale system: Region I (red) contains the core of the screw dislocation (dark red marked by D); Region II (blue) consists of atoms treated with EAM; and the boundary (**B**) region (green) consists of atoms on the boundary between regions I and II. Periodic boundary conditions are used along the ⟨111⟩ dislocation line.

In the present approach, the interaction energy is calculated using the classical EAM potential, i.e.,

$$E^{int}[I, II] = E_{EAM}[I+II] - E_{EAM}[I] - E_{EAM}[II] \quad (6)$$

This of course represents an approximation to E^{int} which stipulates the interaction energy be calculated *only* at EAM level, the same as $E_{EAM}[II]$. The approximation is reasonable because most of the atoms in a typical system are in region II and thus are described by EAM. Although more sophisticated methods, such as orbital-free DFT, could be used to calculate E^{int}, the ensuing computational effort would be much greater.[30] In other words, the present approach represents a reasonable compromise between accuracy and computational time.

This choice of the interaction energy results in a total energy of the form,[30, 38]

$$E[I+II] = E_{EAM}[I+II] - E_{EAM}[I] + E_{DFT}[I] \quad (7)$$

where $E_{EAM}[I+II]$ is the energy of the entire region calculated from the EAM, and $E_{EAM}[I]$ and $E_{DFT}[I]$ are the energies of Region I in the absence of II obtained by EAM and DFT calculations, respectively.[38, 39] The advantage of the formulation is its simplicity. It demands nothing beyond what is required for a DFT cluster calculation and two EAM calculations (one for bulk and the other for a cluster). A major practical advantage of this approach is that, if region I contains several atomic species while region II contains only one atom type, there is no need to have a classical potential for each species and their interactions. This results from the fact that if the various species of atoms are well within region I, then the energy contributions of these atoms cancel out in the total energy calculation (the first two terms in Eq. (7)). Thus, this concurrent approach is particularly useful in dealing with impurities, which is an exceedingly difficult task for classical simulations.

The forces on the atoms in region II (derivatives of Eq. (7) with respect to the nuclear coordinates, $\mathbf{R}^{II}$, in region II) are identical to the forces on these atoms if the EAM potential were used for the entire system; that is to say, as far as forces are concerned, DFT atoms act as if they were EAM atoms. On the other hand, the forces on DFT atoms in region I are

$$\mathbf{F}_i[I] = -\frac{\partial E[I+II]}{\partial \mathbf{R}_i^I} = \mathbf{F}_i^{EAM}[I+II] - \mathbf{F}_i^{EAM}[I] + \mathbf{F}_i^{DFT}[I]$$
$$(8)$$

If the cutoff length of the EAM potential is r_c, then those atoms in region I whose distance from the boundary is larger than r_c will experience a force entirely from $\mathbf{F}_i^{DFT}[I]$. Although these DFT atoms do not feel the presence of the EAM atoms, there are still errors in the force and position of these atoms due to the presence of the fictitious surface inherent in the cluster calculations of region I. On the other hand, the force on the DFT atoms that are within distance r_c from the boundary has contributions both from

$\mathbf{F}_i^{\text{DFT}}[\text{I}]$ and $\mathbf{F}_i^{\text{EAM}}[\text{I}+\text{II}] - \mathbf{F}_i^{\text{EAM}}[\text{I}]$. Thus, the errors in the force (ghost forces) on these DFT atoms are due to (1) the force mismatch between the DFT and EAM calculations, and (2) the fictitious surface effects. It has been demonstrated[30] that in Al, the maximum and average force error on the DFT atoms are 0.45 eV/Å and 0.33 eV/Å, respectively. The corresponding errors on the atomic positions are 0.12 Å and 0.07 Å, respectively.

In order to improve the coupling between regions I and II, we have proposed the following simple correction to the original approach.[38] A third region, referred to as the boundary region is introduced, as shown in Figure 1, which consists of several layers of DFT boundary (B) atoms next to the DFT/EAM boundary. As shown below, although the boundary DFT atoms are included in the DFT cluster calculations of $E_{\text{DFT}}[\text{I}]$, their positions are actually determined by the EAM *bulk force* calculations. Namely, the atomic positions of the boundary atoms do not suffer from the fictitious surface effects, and they serve as a buffer to protect the inner DFT atoms from being exposed to the fictitious surface at the boundary. These inner DFT atoms are of greater interest to a given problem. For example, they could be the core of lattice defects (such as crack tip, dislocation core, grain boundary or interface), chemical impurities, active site or reaction center, etc, which largely determine the properties of materials. The accurate treatment of these inner DFT atoms is the focal point of the multiscale method presented here. More specifically, the force on the boundary DFT atoms is corrected with the term

$$\mathbf{F}_i^{\text{corr}}[\text{B}] = -\mathbf{F}_i^{\text{DFT}}[\text{B}] + \mathbf{F}_i^{\text{EAM}}[\text{B}] \tag{9}$$

so that the force on the boundary atoms is identical to that derived from the EAM calculations for the entire bulk system (I + II).

$$\mathbf{F}_i[\text{B}] = \mathbf{F}_{i,\text{B}}^{\text{EAM}}[\text{I}+\text{II}] \tag{10}$$

Since the EAM gives satisfactory results for bulk properties (typically EAM potentials are fitted to reproduce bulk properties), the force on these boundary DFT atoms should be rather accurate, provided that they are sufficiently far away from the defect center. On the other hand, the force on the inner DFT atoms is determined according to Eq. (8), as in the original approach of Choly et al.[30] Consequently, the force due to the presence of the fictitious surface is eliminated on the boundary DFT atoms, thus protecting the inner DFT atoms from the fictitious surface. The total energy in the revised coupling scheme needs to be corrected accordingly

$$\tilde{E}[\text{I}+\text{II}] = E[\text{I}+\text{II}] - \sum_{i \in \mathbf{B}} \mathbf{F}_i^{\text{corr}}[\text{B}] \cdot \mathbf{u}_i[\text{B}] \tag{11}$$

where $\mathbf{u}_i[\text{B}]$ is the displacement of a boundary atom at each relaxation step, and the sum is over all boundary atoms (B). It is clear from Eq. (11) that the force on region

II atoms and inner DFT atoms is not affected by the correction. This energy correction is similar to that of ghost force in quasicontinuum approach.[29] As will be shown below, this simple correction can significantly reduce the force errors on both DFT and EAM atoms, with no additional computational effort.

The equilibrium structure of the entire system is obtained by minimizing the total energy in Eq. (11) with respect to all degrees of freedom. Because the time required to evaluate $E_{\text{DFT}}[\text{I}]$ is considerably more than that required to compute the EAM energetics, an alternate relaxation scheme turns out to be rather efficient. The total system can be relaxed using the conjugate gradient approach on the inner DFT atoms alone, while fully relaxing the EAM atoms in region II and the boundary atoms. Following Choly et al., an auxiliary energy function that only depends on the inner DFT positions can be defined as

$$E'[\mathbf{R}^{\text{I}}] \equiv \min_{\{\mathbf{R}^{\text{II}},\text{B}\}} \tilde{E}[\mathbf{R}^{\text{tot}}] \tag{12}$$

The significance of E' is that its gradient with respect to $\mathbf{R}_i^{\text{I}}$ can be easily evaluated:

$$\frac{\partial E'}{\partial \mathbf{R}_i^{\text{I}}} = \frac{\partial \tilde{E}[\mathbf{R}^{\text{tot}}]}{\partial \mathbf{R}_i^{\text{I}}} + \sum_j \frac{\partial \tilde{E}[\mathbf{R}^{\text{tot}}]}{\partial \mathbf{R}_j^{\text{II}}} \frac{\partial \mathbf{R}_{j,\min}^{\text{II}}}{\partial \mathbf{R}_i^{\text{I}}}$$

$$= \frac{\partial \tilde{E}[\mathbf{R}^{\text{tot}}]}{\partial \mathbf{R}_i^{\text{I}}}, \tag{13}$$

where the second term on the right hand side of the first equation vanishes because all derivatives are evaluated at the minimum of $\tilde{E}[\mathbf{R}^{\text{tot}}]$ with respect to $\mathbf{R}^{\text{II}}$. The introduction of E' allows for the following relaxation algorithm in the present method:

(i) Minimize $\tilde{E}[\mathbf{R}^{\text{tot}}]$ with respect to $\mathbf{R}^{\text{II}}$ and the boundary DFT atoms while holding the inner DFT atoms fixed. This step involves only the EAM calculations;

(ii) Calculate $\min_{\{\rho^{\text{I}}\}} E_{\text{DFT}}[\rho^{\text{I}}; \mathbf{R}^{\text{I}}]$ and $E_{\text{EAM}}[\mathbf{R}^{\text{I}}]$, and the forces on the inner DFT atoms;

(iii) Perform one step of a gradient-based minimization of E' on the inner DFT atoms; and

(iv) Repeat the process until the entire system is relaxed.

In this way, the number of DFT calculations is greatly reduced, albeit at the expense of more EAM calculations. The total number of DFT energy calculations for the relaxation of an entire system is about the same as that required for DFT calculations for the relaxation of region I alone.

We have compared the improved approach with the original one for the case of bulk Al. The system consists of $6 \times 6 \times 6$ cubic unit cells (4 atoms per cell) of crystalline fcc Al. Region I comprises the innermost 108 ($3 \times 3 \times 3$) atoms, and all other atoms are in region II. The first shell of DFT atoms is selected as boundary atoms. For each relaxation step, a DFT cluster calculation is performed for region I whereas two separated EAM calculations are carried out, one for the entire system (I + II) and the other

6

J. Comput. Theor. Nanosci. 7, 1–30, **2010**

solely for region I. Note that the first EAM calculation employs the periodic boundary conditions, while the second EAM calculation is non-periodic (cluster calculation). The system was initially arranged in the perfect fcc lattice configuration, and then was allowed to relax. Because the EAM potential used in the calculations[42] gives a lattice constant of 3.986 Å, which is slightly smaller than the corresponding DFT value of 3.990 Å, we have scaled EAM potential so that the lattice constant from the EAM potential matches exactly the DFT value. Obviously, if the coupling between region I and region II works perfectly, the entire system would simply behave like ideal bulk Al, i.e., the system will not relax at all because the force on all atoms vanishes. On the other hand, non-zero displacements from the initial equilibrium positions are indications of coupling errors. In Table I, we present the maximum relaxation displacements from the perfect lattice positions for both the boundary and the inner DFT atoms in region I, for the EAM atoms in region II, as well as the corresponding average value.

For the boundary DFT atoms in region I and the EAM atoms in region II, the maximum displacements are reduced by more than one order of magnitude with the improved coupling method. The maximum displacements on the inner DFT atoms and the average atomic displacements in both regions are also significantly decreased. The displacements on the inner DFT atoms can be further reduced if more layers of boundary atoms are included. This however requires region I be large enough so that the inner DFT atoms are well separated from the boundary. Nevertheless, the improved coupling method allows a systematic reduction of coupling errors at reasonable computational expense. The detailed comparison of atomic displacements in region I before and after the force correction is shown in Figure 2.

2.2. Sequential Multiscale Approaches

In this Section we describe two different sequential multiscale approaches. The first is a hybrid *ab initio*-based approach of the atomic-row (AR) model of Suzuki[43] which allows the study of the dislocation core of a screw dislocation in bcc metals. It serves as a link

Table I. Comparison of the maximum displacements from the perfect lattice positions for atoms in region I and region II, without and with the force correction on the boundary atoms. We also list the average displacements for atoms in region I (Δu_{av}^{I}) and region II (Δu_{av}^{II}) without and with the force correction.

	Without correction (Å)	With correction (Å)
Boundary atom	0.07	0.0014
DFT atom in I	0.05	0.003
(Δu_{av}^{I})	0.03	0.0007
EAM atom in II	0.005	0.002
(Δu_{av}^{II})	0.007	0.0003
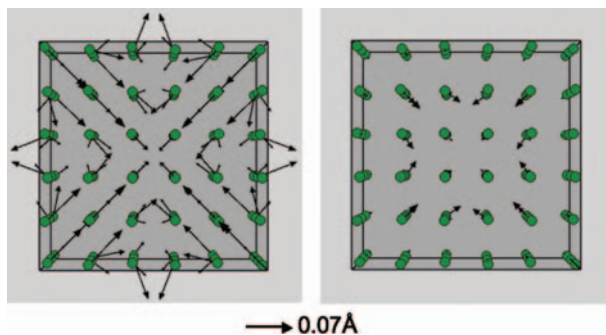
Fig. 2. Displacement vectors of DFT atoms in region I without (left) and with (right) the force correction on the boundary atoms for bulk Aluminum. The length of the arrow represents the magnitude the displacement vector. The same scale is used in both figures.

between *ab initio* and atomistic approaches, and represents a compromise between computationally efficiency and accuracy. The inter-row potential (IRP), derived from *ab initio* calculations, allows the treatment of solutes in the core, while the dislocation core structure is determined by relaxing the ARs using the IRP,[12] similar to atomistic simulations employing interatomic interactions. The second hybrid approach is based on an extension of the Peierls-Nabarro model to study the dislocation-interface interaction, and integrates the atomistic nature from *ab initio* electronic structure calculations into the parametric dislocation dynamics (PDD) method.[44]

2.2.1. Hybrid Ab Initio-Based Atomic-Row Model

Ab initio calculations of dislocations and dislocation-solute interactions, even though most accurate, are computationally expensive. As a result, most atomistic simulations are based on empirical descriptions of atomic interactions. However, such approaches depend critically on the interatomic potentials which are determined by fitting to experimental or *ab initio* data, and hence they are limited to describing accurately the effects of alloying.

The IRP, $\Phi^{(Fe-X)}(\tilde{u})$, between two ARs consisting of Fe and X ($X = $ Fe, Cu, Cr) atoms, respectively, is assumed to depend only on the relative displacement, $\tilde{u}$, of the ARs along the dislocation line and is of the form,[43]

$$\Phi^{(Fe-X)}(\tilde{u}) = \frac{\Phi_0^{(Fe-X)}}{[1 - 4\alpha^{(Fe-X)}]}[\cos 2\pi\tilde{u} - \alpha^{(Fe-X)}\cos 4\pi\tilde{u}$$
$$+ \frac{1}{2}[1 - \alpha^{(Fe-X)}]] \qquad (14)$$

Here, $\tilde{u} = u/b$, where u is the relative displacement and b is the Burgers vector. The parameters $\Phi_0^{(Fe-X)}$ and $\alpha^{(Fe-X)}$ are determined from *ab initio* calculations. Note, that the IRP approach neglects the edge component of the displacement field, which is important for the core structure, mobility and kink nucleation.[45] The change in energy, $\Delta E^{(Fe-X)}(\tilde{u})$, per unit length to displace an AR of X atoms

in the core along $\langle 111 \rangle$ relative to a nearest-neighbor (NN) Fe atomic row

$$\Delta E^{(\text{Fe}-X)}(\tilde{u}) = 3[\Phi^{(\text{Fe}-X)}(\tilde{u} - 1/3) + \Phi^{(\text{Fe}-X)}(\tilde{u} - 1/3)] \tag{15}$$

can be evaluated by *ab initio* calculations. The parameters $\Phi_0^{(Fe-X)}$ and $\alpha^{(Fe-X)}$ can then be determined from Eqs. (14) and (15). The change of inter-row energy has been recently used to study the SSS or SSH in Mo when solute atoms are substituted into that row.[11]

Spin-polarized *ab initio* calculations were carried out using the VASP code.[46, 47] The supercell, shown in Figure 3, consists of three atomic layers in the $\langle 111 \rangle$ direction and 12 atoms per layer. The ARs are along $\langle 111 \rangle$ each represented by a circle. We have used a $4 \times 4 \times 8$ k-mesh according to the Monkhorst-Pack scheme.[48] The generalized gradient approximation functional[49] is used to treat the exchange and correlation potential. The Fe-X IRP is determined by substituting one atomic row, denoted by yellow in Figure 3, with the X solute. For the X–X IRP we substitute the central AR and its six NN rows, denoted by yellow, with solute atoms.

In order to model a dislocation using the *ab initio*-based IRP approach, a $a/2\langle 111 \rangle$ screw dislocation is placed at the center of a rectangular cell of 101.4 Å × 87.8 Å × 2.48 Å along the $[1\bar{1}0]$, $[11\bar{2}]$, and $[111]$ directions, respectively. The slab contains 1875 ARs with a periodic length of $1b$ along the dislocation line. The displacements of the two outermost boundary rows of the slab along the $\langle 110 \rangle$ and $\langle 112 \rangle$ directions are held fixed to the elastic solution values during the relaxation process. The initial geometry for the dislocation in pure Fe is the displacement field $\{u_i\}$ from isotropic elasticity theory, which is adequate for bcc Fe (nearly isotropic). Atomic row positions are in turn relaxed by minimizing the total energy

$$E_{\text{tot}} = \frac{1}{2} \sum_{i,j, i \neq j} \Phi^{(\text{Fe}-X)}(u_i - u_j) \tag{16}$$
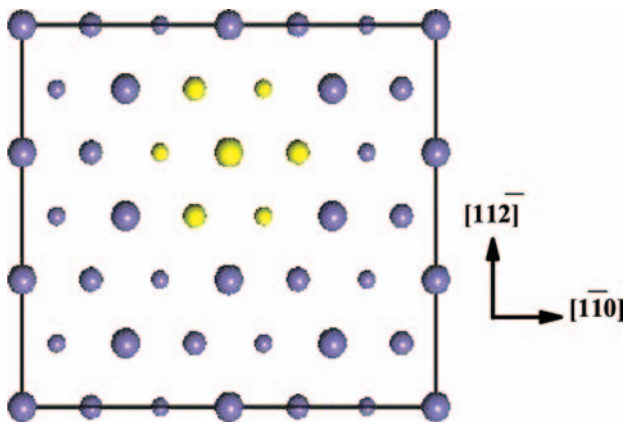
Fig. 3. [111] projection of the supercell used for the calculation of $\Delta E^{(Fe-X)}$. The different circle sizes denote atoms on three successive (111) layers. The Fe atoms are denoted by blue (dark gray), and the solute atoms are denoted by yellow (light gray).

using the conjugate gradient approach. Here, the sum is only over NN ARs.

2.2.2. Hybrid Atomistic-Continuum Approach for Dislocation-Interface Interaction

The mechanical properties of an interface are determined, in large part, by the nature of the chemical bonding at the interface, which may be significantly different from that within either of the materials meeting at the interface. The variation of the generalized stacking fault surface (GSFS) of the interface, the existence of misfit dislocations, and the lattice mismatch can act as barriers to dislocation motion and transmission across the interface. In recent years, there has been considerable interest in the mechanical and structural properties and the deformation mechanisms of metallic multilayer systems, which display remarkably high mechanical strength and hardness comparable to their theoretical strength.[14] The dramatic enhancement of multilayer strength has been generally attributed to the following factors: the mismatch in the elastic properties which results in image forces on the dislocation, the mismatch in the GSFS between incoming and outgoing planes which plays a major role in determining the core properties of the dislocation, the mismatch in the lattice parameters that leads to the generation of coherency stress across the interface, and the GSFS of the interface which may suppress or enhance the spreading of the dislocation core from the glide plane to the interface. Additionally, the existence of misfit dislocations affects the overall strength of multilayers as a result of their mutual interaction with glide dislocations.

Continuum elasticity approaches have been developed for both *welded* and *slipping* interfaces.[50] Recently, Han and Ghoniem[51] have developed a Green's function approach for the elastic field of three-dimensional dislocation loops in anisotropic multilayer materials. As expected, the image force, which is accurately described by linear elasticity,[52, 53] diverges in the vicinity of the dislocation core. In order to overcome this difficulty, an arbitrary cutoff radius, r_0, is generally introduced but its actual value is highly uncertain. Consequently, important quantities, such as the critical stress required to make the dislocation cross the interface, are not accurately determined unless r_0 is calibrated with atomistic calculations.

On the other hand, molecular dynamics (MD) simulations have been used extensively to study different deformation mechanisms in bimaterials. The MD simulations of Hoagland et al.[54] have shown that coherency stresses and interface dislocations play a critical role in determining how the layered microstructure behaves under an applied load. The MD simulations of Rao and Hazzledine demonstrated[55] that a screw dislocation in Cu forms interfacial dislocations in the Cu/Ni twinned interface and hence prefers to spread on the interface rather than to transmit

to Ni. Other MD simulations have also indicated that the intrinsic resistance to slip transmission for Cu/Nb system can originate from the low shear strength of the interface.[56] Although MD simulations are very useful in revealing the atomistic mechanism for the strengthening effect in mulilayers, they suffer from the lack of reliable empirical potentials for treating interatomic interactions across the interface,[57] especially when one considers new materials for which empirical interatomic potentials are not available.

Over the past few years, the PN model combined with ab initio-determined GSFS have been used to study the dislocation core properties in bulk materials[57–60] and the effect of chemistry on the dislocation core properties in aluminum.[61] The GSFS represents the two-dimensional energy profile when the two crystal halves above and below the glide plane are shifted rigidly against each other by a constant disregistry vector, **u**. The GSFS-based approach is essentially a local formulation of the PN model and it assumes the displacement field to be smooth. For a dislocation with a wide core as in the case of Cu and Ni, the strain gradient is relatively small, and therefore, the local formulation should give a reasonable description of the dislocation core structure. Although a non-local formulation of the PN model has been proposed,[62] it has not been widely used due to its complexity.

Anderson et al.[63–65] have extended the PN model to investigate the transmission of a screw dislocation across a coherent, slipping bi-material interface. Anderson and Li[63] and Shen and Anderson[65] developed a 2D PN model for the transmission of a screw dislocation across a slipping and welded interfaces. Their models were able to predict several trends that give more insight to understanding the strengthening mechanisms in bimetallic materials. A general observation made is that slipping interfaces delocalize and trap the core of an incoming dislocation. In spite of its usefulness, Anderson's model suffers from two shortcomings: First, rather than using an *ab initio* description of the atomistic shear on both the glide and interface planes, it employs a simple sinusoidal form of the γ surface which in turn does not allow dissociation. Second, the possibility of a pure screw dislocation to dissociate with a Burgers vector containing an edge component is neglected due to mathematical difficulties. The present model is similar to that of Anderson and Li,[63] and makes use of *ab initio* and the PDD computations to resolve these two issues.

We have developed[66] an extension of the PN model which integrates the atomistic nature from *ab initio* electronic structure calculations into the PDD method.[44] The GSFS provides a two-dimensional representation of the stacking fault energy at zero temperature. Both coherent and incoherent interfaces are considered and the lattice resistance of dislocation motion is captured through the *ab initio*-determined GSFS. In this study, the core properties of a pure screw dislocation as it moves from Cu to Ni are investigated. The effects of the GSFS of the

interface on dislocation core spreading and on the transmission stress is also determined. Additionally, the effect of pre-existing misfit dislocation on interfacial strength and dislocation core spreading is investigated.

The PN model used in this work[66] is an extension to the parametric dislocation dynamics model for bulk materials developed by Banerjee et al.,[22, 23] the so-called generalized PN (GPN) model. In this approach, the full dislocation is represented by a set of N fractional Volterra dislocations with fractional Burgers vector $db = b/N$. A right handed coordinate system as shown in Figure 4 is used. The line of the screw dislocation is along the z direction, and a sufficient amount of edge components is added by introducing N/2 positive and N/2 negative fractional edges (Fig. 4(b)).

In contrast to the treatment of Anderson, the atomic displacements of the dislocation have components in all three directions rather than only along the direction of the Burgers vector. The displacement components of the slip u_x and u_z are determined from the positions of the fractional dislocations of the edge and screw type with fractional Burgers vector. The equilibrium structure of the dislocation core is obtained by seeking the equilibrium configuration of the fractional dislocations. Physically, this corresponds to balancing the elastic force and the lattice restoring force for each infinitesimal dislocation across the glide plane. For a mixed dislocation with components (b^e, b^s) the displacement components can be approximated as

$$u^e(x) = u_x(x) = \sum_{i=1}^{N} b_i^e \tan^{-1}(x - x_i) + \frac{b^e}{2} \qquad (17)$$
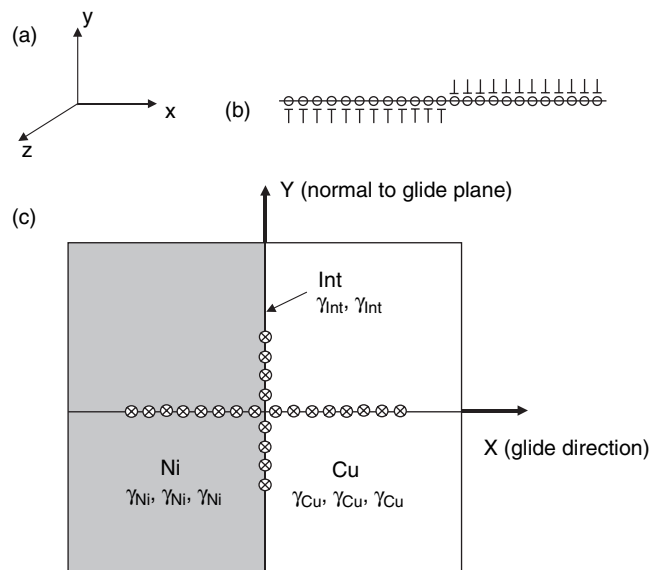
Fig. 4. (a) Coordinate system used in the simulations, (b) Schematic showing the concept of adding extra positive and negative edge components for the pure screw dislocation, (c) Schematic of the discretized Peirels screw dislocation during the transmission process from Cu to Ni. The Burgers vector and the line sense of the dislocation are along the z direction. The fractional Burgers vector is b_{Cu}/N in Cu, b_{Ni}/N in Ni, and $b_{Ni}/2N + (b_{Cu}-b_{Ni})/2N$ in the interface.

and

$$u^s(x) = u_z(x) = \sum_{i'=1}^{N} b_{i'}^s \tan^{-1}(x - x_{i'}) + \frac{b^s}{2} \quad (18)$$

Here, $b_i^e = b^e/N$ and $b_{i'}^s = b^s/N$ are the Burgers vectors of the fractional dislocations, N is the total number of dislocations of edge and screw type, and x_i and $x_{i'}$ denote their corresponding positions. The net elastic force resulting from the interaction between these fractional dislocations is balanced against the lattice restoring force derived from the GSFS across the glide plane. In this formulation, the GSFS of Cu, Ni, and the Cu/Ni interface are determined from *ab initio* electronic structure calculations.

The PN model has been modified to investigate the strengthening mechanisms in slipping and rigid Cu/Ni bimaterial. The effects of mismatch in the (1) elastic properties, (2) GSFS, and (3) lattice parameters reflecting the existence of misfit dislocations, are explicitly taken into account. For a slipping interface, part of the dislocation content can be accommodated by the interface through dislocation core spreading. Any dislocation that moves from the glide plane to the interface is divided into two identical fractional dislocations, symmetrically placed with respect to the slip plane. In particular, the mismatch in lattice constant between Cu and Ni is accommodated by the fractional residual slip on the interface. The continuity of the Burgers vector requires that

$$b_{\text{Cu}} = n_{\text{Cu}} db_{\text{Cu}} + n_{\text{Ni}} db_{\text{Ni}} + 2n_{\text{Int}} db_{\text{Int}} \quad (19)$$

where $N = n_{\text{Cu}} + n_{\text{Ni}} + n_{\text{Int}}$, n_{Cu}, n_{Ni}, and n_{Int} are the number of fractional dislocations in Cu, Ni, and the interface, respectively, and $db_{\text{Cu}} = b_{\text{Cu}}/N$, $db_{\text{Ni}} = b_{\text{Ni}}/N$, and $db_{\text{Int}} = b_{\text{Cu}}/2N$.

For the Cu/Ni bimaterial, the equilibrium condition of a fractional dislocation i depends on whether the fractional dislocation is in Cu, Ni or on the interface. The total force on the ith fractional screw dislocation can be expressed as,

$$F_{i,\,\text{Cu}}^s = \left[\sigma_{\text{ext}}^s + \sum_{j=1}^{n_{\text{Cu}}} \sigma_{\text{Cu-Cu}}^s(x_i, x_j) + \sum_{j=1}^{2n_{\text{Int}}} \sigma_{\text{Cu-Int}}^s(x_i, y_j) \right.$$
$$\left. + \sum_{j=1}^{n_{\text{Ni}}} \sigma_{\text{Cu-Ni}}^s(x_i, x_j) \right] b_{i,Cu}$$
$$+ f_{i,\,\text{Cu}}^s + f_{i,\,\text{Cu}}^{\text{coh}} \quad (20)$$

$$F_{i,\,Int}^s = \left[\sigma_{\text{ext}}^s + \sum_{j=1}^{n_{\text{Cu}}} \sigma_{\text{Int-Cu}}^s(y_i, x_j) + \sum_{j=1}^{2n_{\text{Int}}} \sigma_{\text{Int-Int}}^s(y_i, y_j) \right.$$
$$\left. + \sum_{j=1}^{n_{\text{Ni}}} \sigma_{\text{Int-Ni}}^s(y_i, x_j) \right] b_{i,\,\text{Int}}$$
$$+ f_{i,\,\text{Int}}^s + f_{i,\,\text{Int}}^{\text{coh}} \quad (21)$$

$$F_{i,\,\text{Ni}}^s = \left[\sigma_{\text{ext}}^s + \sum_{j=1}^{n_{\text{Cu}}} \sigma_{\text{Ni-Cu}}^s(x_i, x_j) + \sum_{j=1}^{2n_{\text{Int}}} \sigma_{\text{Ni-Int}}^s(x_i, y_j) \right.$$
$$\left. + \sum_{j=1}^{n_{\text{Ni}}} \sigma_{\text{Ni-Ni}}^s(x_i, x_j) \right] b_{i,\,\text{Ni}}$$
$$+ f_{i,\,\text{Ni}}^s + f_{i,\,\text{Ni}}^{\text{coh}} \quad (22)$$

Here x_i, and y_i are the positions of the fractional dislocations on the glide and the interface planes, respectively. The first term σ_{ext}^s in each equation is the externally applied stress along the dislocation line; the second, third and fourth terms are the stress exerted on the fractional dislocation from other fractional dislocations located in Cu, on the interface, and in Ni, respectively; the fifth term is the lattice restoring force derived from the GSFS, and the last term is the coherency stress. The expressions for the stress in the above equations are normalized with respect to the average shear modulus $\bar{\mu} = (\mu_{\text{Cu}} + \mu_{\text{Ni}})/2$. Note, that the fourth term, $\sigma_{\text{Cu-Ni}}^s$, in Eq. (20) and the second term, $\sigma_{\text{Ni-Cu}}^s$, in Eq. (22) represent the image stresses (Koehler stresses) resulting from the misfit in the elastic properties between Cu and Ni. The explicit expressions of the image stress for the screw and edge components are given in Refs. [53] and [63], respectively.

We assume here that there is no dislocation climb and therefore only screw dislocations can spread out onto the interface. Additionally, the external stress and coherency stress are applied only to the screw components on the glide plane; i.e., $\sigma_{\text{Int}}^{\text{ext}} = 0$ and $f_{\text{Int}}^{\text{coh}} = 0$. The expression for the net force on the ith fractional edge dislocation is similar to those for a fractional screw dislocation in of Eqs. (20) and (22), but with the following differences: no external stress is applied on the edge component and there is no stress contribution from the interface because the fractional edge dislocation is confined to the glide plane.

The edge and screw components of the lattice restoring force, obtained from the GSFS are given by

$$f_i^e = -b_i^e \left. \frac{\partial \gamma}{\partial u^e} \right|_{x=x_i}; \quad f_i^s = -b_i^s \left. \frac{\partial \gamma}{\partial u^s} \right|_{x=x_i} \quad (23)$$

where γ is the GSFS of Cu, Ni, or the interface.

The force due to the coherency stress results from the mismatch in the Cu/Ni lattice parameters. The calculated uniaxial coherency stress in Cu/Ni bimaterial is around 2.5 GPa,[67] which is equivalent to 1.0 GPa when resolved on the glide plane. In this work the coherency stress is assumed to be of a step function centered at the interface with the value $\sigma_i^{\text{Coh}} = \pm 1.0$ GPa, where the plus (minus) sign indicates compressive (tensile) stress in Cu (Ni). It is worth mentioning that the geometry used in the current work assumes that the interfacial (100) plane is perpendicular to the glide plane (111) to avoid additional computational complexities. However, in reality the glide plane is inclined with respect to the interfacial plane by an angle

$\theta = 58.5°$, which in turn leads to asymmetric dislocation core spreading due to the modification of the image forces.

In this quasistatic framework, the dislocation glide is controlled by drag, and hence the dislocation velocity is proportional to the resolved shear stress. Having determined all the force components, the equilibrium position of each fractional dislocation is computed according to the drag dislocation dynamics relation,

$$F_i = B \frac{dx_i}{dt} \qquad (24)$$

where B is a drag coefficient to update the position x_i of the dislocation at each time step until the system reaches equilibrium.

The interfacial strength is determined by computing the critical value of the external stress required to transmit the dislocation from Cu to Ni. The external stress is applied incrementally to push all fractional dislocations across the interface. When the leading dislocation reaches a critical distance of $0.04b_{Cu}$ from the interface, there are two pathways available for the dislocation: it can either spread onto the interface or continue gliding on the original slip plane into Ni. The dislocation will follow the lowest-energy pathway. The process is repeated for all fractional dislocations while the applied stress keeps increasing until it reaches its critical value, $\tau_{critical}$, that allows dislocation transmission.

3. APPLICATIONS

3.1. Core Properties of an Edge Dislocation in Aluminum

The computation of the Peierls stress in Al represents a difficult task because of its extremely low value. Numerical uncertainties arising from the application of boundary conditions, interatomic potentials and interpretation of the results could be comparable to the value of the Peierls stress itself. Hence, there have been large discrepancies in the theoretical/computational estimates of the Peierls stress in Al. On the experimental side, the situation is not better—the two orders of magnitude discrepancy between the Peierls stress estimated from internal friction measurements and from mechanical testing has been tantalizing for decades.[68, 69] Since the concurrent multiscale method contains an accurate description of the dislocation core via DFT along with a reliable long-range elastic field provided by EAM, one would expect that it will give a more reliable estimate of the Peierls stress compared to previous studies.

We have applied the improved coupling method to study the core structure and mobility of an edge dislocation in Al. Dislocations are good test for multiscale approaches because their properties depend both on the atomistic details at the core and the long-range elastic strain field. More importantly, there is a wide range of conflicting experimental and theoretical results on the Peierls stress of dislocations in Al. Theoretical values range from $10^{-5}\mu$ to $10^{-4}\mu$ for an edge dislocation, and experimental measurements span from $2.7 \times 10^{-5}\mu$ to $10^{-3}\mu$, where $\mu = 26$ GPa is the [110] shear modulus of Al obtained from the scaled EAM calculation. The shear modulus agrees very well with the DFT value of 27 GPa. These discrepancies have led to various suggestions, such as the existence of a multiple core structures[70] or the interaction of vacancies with the dislocation core.[71] Therefore it is of scientific interest to revisit the problem by multiscale modeling.

We consider an edge dislocation with a Burgers vector $a/2[110]$ in Al ($\alpha = 3.990$ Å). The dimensions of the entire system are 237 Å $\times$ 37 Å $\times$ 4.86 Å and those of region I are 30 Å $\times$ 15 Å $\times$ 4.86 Å. The dislocation line is along the $[\bar{1}12]$ (z) direction and the glide direction is along the $[110]$ (x) direction, and hence the glide plane (xz) is $(1\bar{1}1)$. There are 126 DFT atoms in region I and 2748 EAM atoms in region II. One layer of DFT atoms in region I that are adjacent to EAM atoms in region II is chosen as boundary atoms. All atoms are initially displaced according to the anisotropic elastic solution of the dislocation. The boundaries along the x and y axis are held fixed to the elastic solution values during the relaxation process. Periodic boundary conditions are applied along the z direction to simulate a straight dislocation. The DFT calculations for region I are performed using the plane-wave pseudopotential VASP package[46, 47] with a cluster of a 8 Å vacuum along both $\pm x$ and $\pm y$ directions. The energy cutoff for Al is 129 eV. We find that $8k$ points along the one-dimensional Brillouin zone are adequate for good convergence.

The dislocation core structure is summarized in Figure 5. The top panel shows the relative atomic displacement across the glide plane along the x (solid line) and z (dashed line) directions, corresponding to the edge and screw components of the displacement field, respectively. The corresponding dislocation density (the derivative of the relative displacement with respect to x) is presented in the lower panel. The double-peak in the dislocation density plot suggests that the dislocation is dissociated into two Shockley partials whose positions are represented by the peaks. The partial separation distance of 5.9 Å is smaller than the corresponding value from EAM simulations of 9 Å.[72] The experimental measurement of the partial separation is about 5.5 Å.[73] The dislocation core width, which is defined as the atomic distance over which the x-relative displacement changes from $(1/4)b$ to $(3/4)b$, is 5.5 Å.

Because of its extremely low value, the theoretical determination of the Peierls stress in fcc metals has been challenging. The computational errors arising from the inaccuracy of the interatomic potentials, the deficiencies of continuum-based models, and the improper use of boundary conditions[74] can easily reach or exceed the magnitude of the Peierls stress itself. To determine the Peierls stress
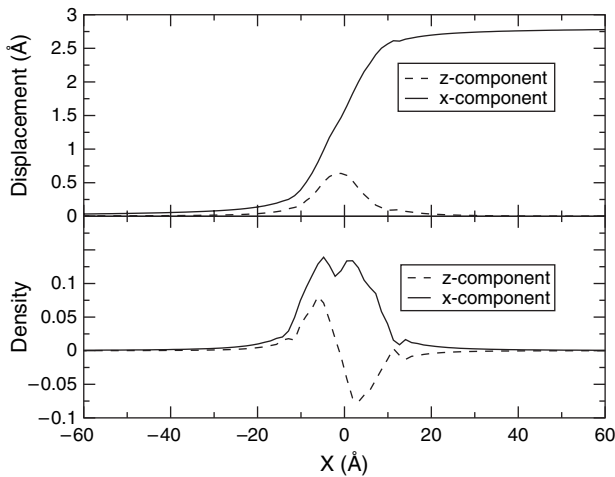
Fig. 5. Top panel: the x-component (solid line) and z-component (dashed line) of the relative atomic displacement, corresponding to the edge and screw components of the displacement field, respectively, as a function of x. Bottom panel: the x component (solid line) and z component (dashed line) of the Burgers vector density as a function of the x coordinate. The double-peak structure in the density plot illustrates the dislocation dissociation into partials.

with the present method, we apply periodic boundary conditions along both x and z directions. Note that this is different from the core structure calculations, where fixed boundary conditions were applied along the x direction. The advantage of using periodic boundary conditions along x, is that the Peach-Koehler forces acting on any of the dislocations arising from their periodic images cancel identically due to the translational symmetry along x, whereas the fixed boundary conditions introduce fictitious forces from the boundary walls. The external force on the top-layer atoms is gradually increased along the x direction, while holding the bottom-layer atoms fixed and relaxing the rest of the system using the conjugate gradient method described above. The applied external force on each atom is given by the desired applied shear stress multiplied by the area per atom. The dislocation center is determined from the x position where the screw component of the dislocation density changes sign. We find that the dislocation center starts moving at the shear stress of $2.5 \times 10^{-3}\ \mu$, and the center displacement reaches about one Burgers vector (~ 2.86 Å) under the shear stress of $7.5 \times 10^{-3}\ \mu$. According to the definition of Peierls stress introduced earlier, we estimate the Peierls stress to be $7.5 \times 10^{-3}\ \mu$, in good agreement with the experimental value of $8 \times 10^{-3}\ \mu$ of Bujard and coworkers.[75] A similar result was obtained by applying the shear stress simultaneously on both the top- and bottom-layers. It should be noted that the present calculations of the Peierls stress represent a preliminary result, and further studies by other *ab initio*-based multiscale methods, such as in Ref. [37], are needed to ascertain the precise value of the Peierls stress.

For comparison, we have also performed EAM calculations for the entire system. The Peierls stress thus obtained

is about $4.5 \times 10^{-4}\ \mu$, which is an order of magnitude smaller than the corresponding value derived form the present multiscale method. Moreover, the dislocation core width is about three times larger than that from the multi-scale simulations. Therefore the lower value of the Peierls stress obtained from the EAM calculations is consistent with the fact that the Peierls stress is smaller for a wider dislocation.

Finally, we have calculated the Peierls stress by following the method introduced by Wang et al.[72] which uses fixed boundary conditions along the x direction. In Wang's approach, the applied shear stress, τ, as a function of the dislocation translation, u, is written as

$$\tau(u) = Ku + \tau_1 \sin\left(\frac{2\pi u}{d}\right) + \tau_2 \sin\left(\frac{4\pi u}{d}\right) \qquad (25)$$

where K is a constant representing the magnitude of the image force caused by the fixed boundaries, d is the period of the Peierls potential which is the Burgers vector for an edge dislocation, and τ_1 and τ_2 are constants. The Peierls stress corresponds to the maximum value of the sum of the last two terms in Eq. (25). The results (open circles) of the applied shear stress as a function of the dislocation translation are shown in Figure 6. The solid curve in the figure, which is a least-square fit of the data to Eq. (25), yields a Peierls stress of $0.036\ \mu$, which is an order of magnitude higher than the value of $7.5 \times 10^{-4}\ \mu$ obtained from the multiscale approach, suggesting that Eq. (25) may not be generally applicable.

3.2. Chemistry Effect on Dislocation Mobility in Refractory bcc Metals

Continuum elasticity theory has provided considerable insight in describing the long-range effects associated with
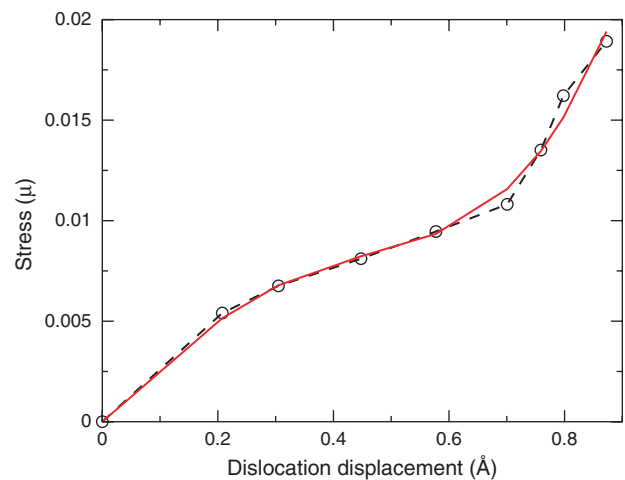
Fig. 6. Applied shear stress as a function of the dislocation translation (open circles). The solid curve is the least-square fit of the simulation data to Eq. (25), which yields a Peierls stress of about $0.036\ \mu$. The dashed curve is a guide to the eye.

mismatch in size and elastic constants between the solute and host atoms. On the other hand, in their pioneering work, Trinkle and Woodward[11] using the first-principles Greens function boundary condition (FP-GFBC) method,[37] demonstrated that the transition-metal solutes can have a dramatic effect on the dislocation core and hence the mobility. This non-linear short-range dislocation-solute interaction is purely of *chemical* or electronic origin.[11, 12] Nevertheless, the understanding of the physics of interactions of dislocations with nano-clusters remains a challenging problem.

In this section, we apply the novel concurrent multiscale approach, described in Section 2.1 to study the effects of chemistry and local environment on the mobility of dislocations including the Peierls stress and Peierls potential in Ta–W alloys. This approach treats correctly the long-range elastic field of the dislocation and describes the solute-host atomic interaction in the core region accurately. The results demonstrate the dual nature of W solutes: depending on the solute local environment (random solid solution or nano-clusters of different geometry and composition), the mobility and/or Peierls potential may exhibit a wide spectrum of unusual behavior: SSH, SSS or even a disappearance of the Peierls potential resulting in a spontaneous dislocation glide in the absence of external stress. Finally, W solutes can serve as obstacles to dislocation motion and activate new slip planes.

The size of the entire system is 251 Å × 145 Å × 2.86 Å along the ⟨110⟩, ⟨112⟩, and ⟨111⟩ directions, respectively, containing 5,400 atoms. Region I is 22 Å × 28 Å × 2.86 Å and contains 96 atoms. All atoms are initially displaced according to the isotropic elastic solution of the screw dislocation with Burgers vector $\vec{b} = \langle 111 \rangle a/2$, and are then relaxed by the concurrent multiscale approach, which takes into account the anisotropic effects. Periodic boundary conditions are applied along the ⟨111⟩ direction and fixed boundary conditions are employed along the other two directions, respectively. The DFT cluster calculations in region I were carried out using the VASP code.[46, 47] We have used a $1 \times 1 \times 8$ k-mesh according to the Monkhorst-Pack scheme.[48] The generalized gradient approximation functional[49] is used to treat the exchange and correlation potential, and the cutoff energies are set at 240 eV for both Ta and W. The EAM calculations employed the Ackland potential[76] for pure Ta and the Johnson scheme[77] for constructing the Ta–W interatomic potential. It should be emphasized that the quality of the Ta–W classical interaction is not crucial in this multiscale approach, due to the cancelation between the first two energy terms in Eq. (7), provided that the various atomic species are well within region I. The external stress is applied by displacing equally the atoms in the outermost $(10\bar{1})$ and $(\bar{1}01)$ planes along the $[\bar{1}\bar{1}\bar{1}]$ and $[111]$ directions, respectively. The corresponding shear stress, σ_{yz}, is calculated as the component of the area-averaged force on the surfaces parallel to the Burgers vector.
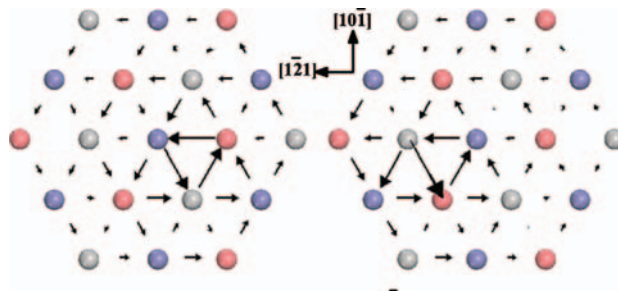
Fig. 7. DD map of the core of the screw dislocation in Ta under (a) zero stress (left panel), and (b) 1.8 GPa (right panel). Circles of different color represent atoms on three successive (111) planes.

In Figure 7 we show the relaxed dislocation core structure in pure Ta under zero stress (left panel) and 1.8 GPa (right panel), respectively, using the differential displacement (DD) maps.[78] The arrows indicate the relative [111] displacement of neighboring atoms of the dislocation. The length (direction) of the arrow denotes the magnitude (sign) of the displacement difference. When the arrow touches the centers of the two atoms, their relative displacement is $b/3$. The dislocation core for pure Ta is nondegenerate and spreads symmetrically on the six planes. Upon increasing the shear stress σ_{yz} applied on the $(10\bar{1})$ planes, the dislocation center moves to the next Peierls valley at the critical stress σ_P of 1.8 GPa. Comparison of σ_P and the core structure in Table II employing different approaches, demonstrates that the concurrent multiscale approach is in excellent agreement with the results of the FP-GFBC method.[37]

In order to study the effect of local environment of the solute on the mobility of the screw dislocation we have considered the cases of: (1) dilute random solid solutions where the dislocation line is affected only by isolated solute atoms (ISA) shown in Figure 8(a), and (2) small clusters of solute atoms of hexagonal shape (CSA-H) shown in Figure 8(b) or of triangular shape (CSA-T) shown in Figure 8(c). In all cases the W concentration is ∼ 6 at.% and the W atoms are denoted with black circles. The upward triangle, downward triangle, square, and solid dot denote the position of the dislocation center under 0.0, 1.0, 1.5, and 2.0 GPa, respectively. In the absence of stress the core center is at point Γ in panel (d) for the ISA and the CSA-T cases, while it is unstable [dashed red cross in panel (b)] for the CSA-H case. Interestingly, in the latter case the dislocation center is repelled by the CSA-H

Table II. Peierls stress (σ_P) and core structure for a screw dislocation in Ta using the present multiscale approach, the FP-GFBC method, the EAM, and the modified generalized pseudopotential theory (MGPT).

	σ_P (GPa)	Core structure
Present work	1.8	Nondegenerate
FP-GFBC[37]	1.8	Nondegenerate
EAM[79]	1.8	Degenerate
MGPT[80]	0.6	Nondegenerate
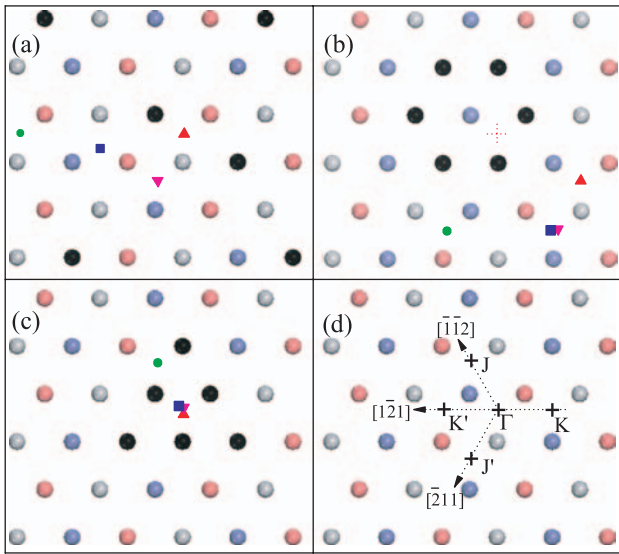
Fig. 8. Screw dislocation slip paths under stress for three configurations of W solutes denoted by black circles: (a) isolated solute atoms (ISA); and nano-clusters of (b) hexagonal (CSA-H) or (c) triangular (CSA-T) shape. The upward triangle, downward triangle, square, and solid dot denote the position of the core center under 0.0, 1.0, 1.5, and 2.0 GPa, respectively. Panel (d) displays the special points and directions in Figure 9. Γ indicates the initial position of the dislocation.

and spontaneously moves to the position of the solid red cross under the precipitate-induced chemical stress. Under 1.0 GPa, both in the ISA and CSA-H cases the dislocation prefers to bypass the W sites and moves on the $(0\bar{1}1)$ plane. Upon increasing the stress to 1.5 GPa, the behavior changes dramatically: the dislocation in ISA continues to move, while it is pinned in CSA-H. The dislocation in CSA-H begins to move further under 1.8 GPa, as in the case in pure Ta. In sharp contrast to the other two cases, the dislocation core is pinned at Γ in the CSA-T case until the stress reaches 2.0 GPa, where the center moves on the $(\bar{1}10)$ glide plane. The calculated values of critical stress, σ_P, and polarization p are listed in Table III, for the ISA, CSA-H, and CSA-T environments. Both ISA and CSA-H result in SSS, while CSA-T produces SSH. In all cases, W solutes have a small effect on the polarization, indicating the absence of correlation between the polarization and σ_P.

Edagawa et al.[81] suggested that the dislocation motion in bcc metals can be represented by the Peierls potential surface (PPS), a 2D surface perpendicular to the Burgers vector. The profile of PPS is a valuable quantity to

Table III. σ_P (GPa) and polarization p for isolated solute atoms (ISA), nano-clusters of solute atoms of hexagonal shape (CSA-H) or of triangular shape (CSA-T), shown in Figure 8.

	ISA	CSA-H	CSA-T
σ_P	1.0	1.0	2.0
p	0.10	0.04	0.00

measure the lattice resistance to dislocation motion. Using the present approach we have determined the PPS by moving the dislocation center along different directions in Figure 8(d). The PPS along the various $\langle 1\bar{2}1\rangle$ directions for pure Ta, the ISA, and the CSA-T environments is shown in Figure 9(a) and the corresponding PPS for CSA-H is shown in Figure 9(b). The Peierls barrier along the $[1\bar{2}1]$ (Γ–K') and $[\bar{2}11]$ (Γ–J') directions are reduced compared to pure Ta, consistent with the results of σ_P in Table III. On the other hand, the CSA-H environment has a dramatic effect on the PPS along the $[\bar{1}2\bar{1}]$ direction, where the Peierls barrier between Γ and K is greatly reduced, which is the reason why the dislocation glides spontaneously (under zero stress) in Figure 8(b). Finally, for the CSA-T configuration, the barrier along $[1\bar{2}1]$ on the $(\bar{1}01)$ plane increases, while that along $[\bar{1}\bar{1}2]$ on the $(\bar{1}10)$ plane remains the same as in Ta. Thus, the dislocation first glides on the $(\bar{1}10)$ plane, which is different from that in pure Ta.

In order to understand the underlying mechanism of the dislocation-solute interaction, we present in Figure 10 the change in energy, $\Delta E^{(X-X)}(u/b)$, per unit length to
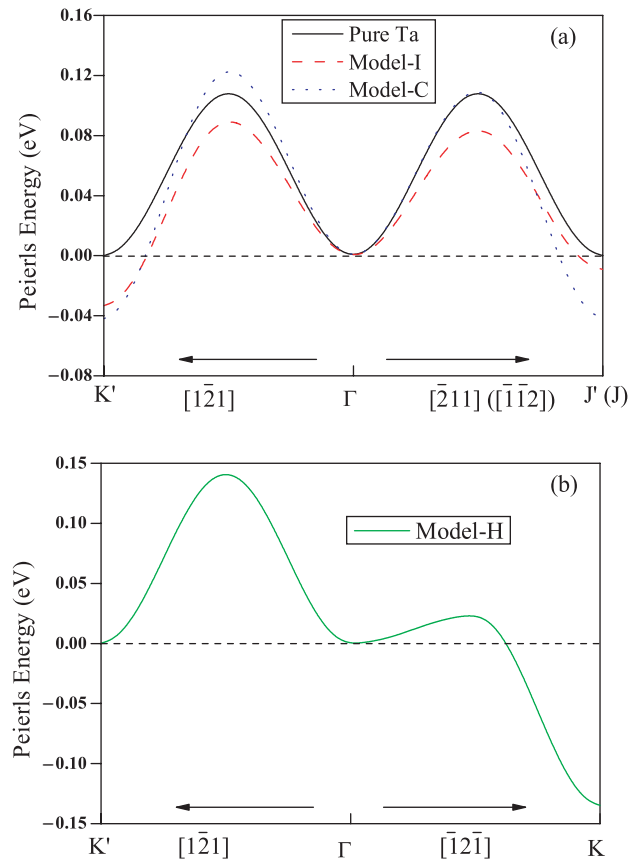
Fig. 9. Peierls potential along the various $\langle 1\bar{2}1\rangle$ directions in Figure 8(d) for: (a) Pure Ta (black solid curve), the ISA (red dashed curve), and the CSA-T (blue dotted curve); and (b) for the CSA-H (green solid curve). The direction and special point in parenthesis in Figure 9(a) correspond to the CSA-T environment.
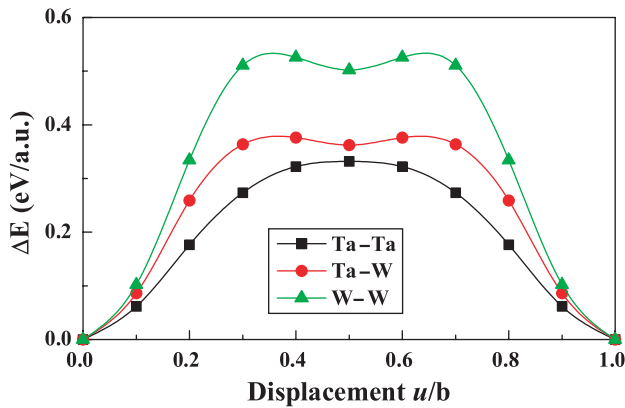
Fig. 10. Energy change per unit length, $\Delta E^{(X-X)}(u/b)$ ($X = $ Ta, W), versus the normalized atomic-row displacement u/b along $\langle 111 \rangle$.

displace an atomic row of X atoms ($X = $ Ta, W) by u along $\langle 111 \rangle$ relative to a nearest-neighbor Ta atomic row.[11, 12, 82] We find that W increases substantially the inter-row shear energies for the Ta–W and W–W rows and the lattice resistance when the dislocation center is in the vicinity of W. This in turn increases σ_P and hence SSH. On the other hand, the dislocation tends to bypass W and changes the slip plane and/or slip direction. This could be achieved by either cross-slip or kink formation. The definitive mechanism requires further study. The interplay between dislocation pinning, cross slip, and kink nucleation is responsible for the multitude of plastic behavior observed in solid-solution alloys.

3.3. Effect of Cu or Cr Nano-Clusters on Dislocation Core in α-Fe

The α-Fe-X base alloys ($X = $ Cr, Cu, Ni, etc.) are ideal systems to study SSH due to the very low solubility of X in Fe at low temperatures and the importance of solute precipitation on the irradiation hardening and embrittlement of low alloy reactor pressure vessel steels.[8, 10] Previously, studies based on empirical interatomic potentials were used to study precipitate interactions in Fe–Cu and have shown that ~3 nm Cu precipitates strengthen α-Fe.[10, 83, 84] However, the origin of the electronic structure responsible for the SSS or SSH in α-Fe remains an unexplored area thus far,[85] because of the inadequacy of empirical potentials.

The purpose of this work is to present a theoretical study of the effect of Cu or Cr solutes and solute-clusters on the dislocation core properties of the $a/2\langle 111 \rangle$ screw dislocation in α-Fe. We employ the *ab-initio*-based atomic-row (AR) approach of Suzuki[43] discussed in Section 2.2.1, whose results are corroborated by complementary atomistic simulations using empirical interatomic potentials. The calculations reveal that Cu nano-precipitates induce a dramatic change in the core structure from non-polarized in pure Fe to polarized. In sharp contrast, it will be shown

that Cr-precipitates have small effect on the core polarization and increase the Peierls stress (σ_P). The underlying atomistic mechanism responsible for these uniquely electronic structure effects will be elucidated here.

Figure 11(a) shows $\Delta E^{(Fe-X)}$ and $\Delta E^{(X-X)}$ versus $\tilde{u}$, for $X = $ Fe, Cu, and Cr. The corresponding IRP, Φ^{Fe-X} and Φ^{X-X} versus $\tilde{u}$ are shown in Figure 11(b). For Fe–Fe, Fe–Cr and Cr–Cr, ΔE exhibits two well-pronounced maxima at $u = b/3$ and $u = 2b/3$, associated with both the bcc structure and the unfilled $3d$ band for Fe and the solute atom. On the other hand, Cu solutes reduce dramatically the atomic-row shear energies for the Fe–Cu and Cu–Cu rows. Moreover, there is a change of the shape of ΔE, which displays a single maximum at $u = b/2$ for both Fe–Cu and Cu–Cu. These results clearly demonstrate that Cu solutes act as lubricants and facilitate the shear process between the Fe–Cu and Cu–Cu rows. Analysis of the density of states and charge density indicate that the NN inter-row interaction for Fe–Fe, Fe–Cr, and Cr–Cr is dominated by t_{2g}–t_{2g} hybridization at the Fermi energy. The stronger bonding between NN Cr pairs compared to Fe pairs results in $\Delta E^{(Cr-Cr)} > \Delta E^{(Fe-Fe)}$. On the contrary, the Fe–Cu and Cu–Cu NN inter-row interactions are dominated by t_{2g}–s hybridization, which being weaker than the t_{2g}–t_{2g}, results in smaller $\Delta E^{(Fe-Cu)}$.

In Figure 12(a) we show the relaxed dislocation core structure for pure Fe employing the differential displacement (DD) maps[45, 78] for the screw component, using the *ab initio*-based IRP approach. The arrows indicate the relative $\langle 111 \rangle$ displacement of neighboring atoms produced by the dislocation. The length of the arrow is proportional to the magnitude of the displacement difference and the direction of the arrow indicates the sign of the displacement difference. When the arrow touches the centers of the two atoms, their relative displacement is $b/3$. The orientation of all the {110} and {112} planes belonging to
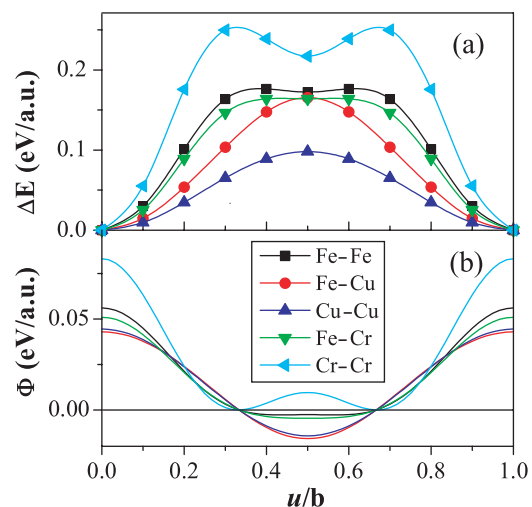
Fig. 11. (a) Energy change per unit length, $\Delta E^{(Fe-X)}$ and $\Delta E^{(X-X)}$ for $X = $ Fe, Cu, and Cr, versus the normalized AR displacement u/b along $\langle 111 \rangle$. (b) Corresponding variation of IRP, Φ^{Fe-X} and Φ^{X-X}.

REVIEW
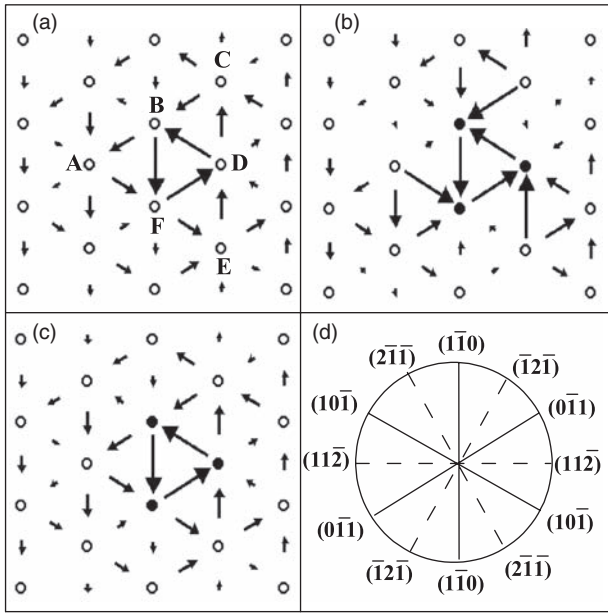
Fig. 12. DD map of the core for a $a/2\langle 111\rangle$ screw dislocation in (a) pure Fe, (b) Fe–Cu and (c) Fe–Cr, calculated from the *ab initio*-based IRP approach. The hollow circles and solid circles represent Fe and impurity atoms, respectively. (d) [111] stereographic projection of all {110} and {112} planes belonging to the [111] zone.

the [111] zone is shown in Figure 12(b). The dislocation core for pure Fe is symmetric (non-degenerate) and spreads symmetrically on the six planes, in agreement with recent fully *ab initio*[86] and atomistic[87] calculations. The core structure for a small Cu cluster composed of three rows along the dislocation core, as shown in Figure 12(b), changes dramatically from symmetric to non-symmetric (degenerate), where the dislocation core spreads primarily into three {110} planes. Thus, the 2.5 Å size Cu cluster reduces the core non-planarity and renders it to more planar. In sharp contrast, the three atomic row Cr precipitate in Figure 12 has a very small effect on the core structure, i.e., the core remains isotropic as in the case of pure Fe.

The change of the core structure induced by the Cu nano-precipitate invites the question what is the core structure of the $a/2\langle 111\rangle$ screw dislocation in pure bcc Cu, with lattice constant of $a_0 = 2.866$ Å. The core structure of the screw dislocation in bcc Cu calculated from the *ab initio*-based IRP method and the Finnis-Sinclair (FS) interatomic potential[88] is shown in Figures 13(a) and (b), respectively. Interestingly, both approaches yield a non-symmetric (degenerate) core structure, similar to that of the Cu nano-precipitate in pure Fe, indicating that the unique inter-row energy profile between Cu atomic rows in Figure 11(a) is responsible for the more planar core structure.

To quantify the effect of chemistry on the core structure of Fe, we have calculated the core polarization, p,[79]

$$p = \frac{|d_{AB} - d_{BC}| + |d_{CD} - d_{DE}| + |d_{EF} - d_{FA}|}{b} \qquad (26)$$
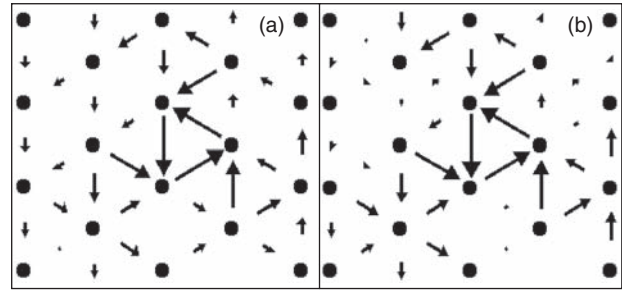
Fig. 13. DD Map for the core structure for a $a/2\langle 111\rangle$ screw dislocation in pure bcc Cu using the (a) *ab initio*-based IRP approach and (b) the FS potential, respectively.

Here, $d_{i,j}$, (i, j = A, B, C, D, E, or F) is the relative displacement between two neighboring atoms in the two columns denoted as i and j in Figure 12(a). Thus, a symmetric core leads to $p = 0$, while $p = 1$ corresponds to a fully asymmetric core. In Table IV we list the polarization of the dislocation core as a function of the number of solute ARs. The polarization increases with increasing Cu concentration, indicating that the Cu–Cu NN atomic pairs play a significant role on the dislocation core, as pointed out empirically by Tapasa et al.[89] On the other hand, the polarization is almost independent of the Cr concentration, as is also evident in Figure 12(c). It is important to emphasize that due to the small size of the solute precipitate, the change of polarization induced by Cu cannot be attributed to the elastic modulus mismatch between Cu and Fe. Rather, it is purely a "chemistry effect" whose origin lies in the different (similar) electronic structure between Cu (Cr) and Fe, and the change of $3d$–$3d$ hybridization in pure Fe or Fe–Cr system to the $43d$–$4s$ hybridization in the Fe–Cu system. One should expect a similar effect with other simple-metal alloying elements.

Since the core polarization is a controlling factor of dislocation mobility,[45, 90] one would expect that under external stress, the polarized core in Fe–Cu will behave differently from the non-polarized one in pure Fe. In order to corroborate the results of the *ab initio*-based inter-row approach and to study the effect of external stress, we have carried out also static atomistic simulations at zero temperature based on the embedded atom method. Moreover, the atomistic simulations include atomic displacements perpendicular to $\langle 111\rangle$ (edge component), which even though small, they are important in kink formation and in lowering σ_P.[45] We have employed the interatomic potentials in Ref. [76] for pure Fe, and in Ref. [88] for the

Table IV. Polarization, p, of the screw dislocation core, defined in Eq. (26), as a function of the number of solute AR, using the *ab initio* IRP approach.

No. impurity atoms		0	1	2	3
p	Cu	0.00	0.11	0.48	0.99
	Cr	0.00	0.01	0.02	0.00
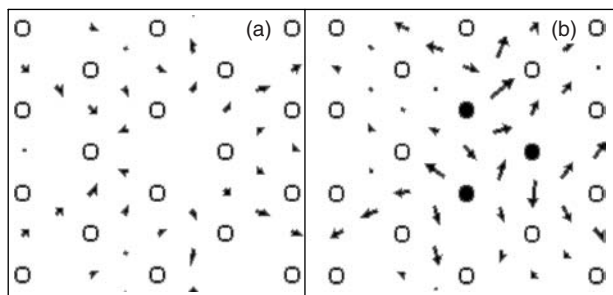
Fig. 14. DD map of the edge component of the dislocation core for (a) pure Fe and (b) Fe–Cu using the atomistic simulations based on the FS potential. The vectors have been magnified by a factor of 5 to make them clearly visible.

Fig. 15. DD map of the screw dislocation core for Fe–Cu under pure shear stress of (a) 0.8 GPa, and (b) 1.5 GPa, respectively by using EAM. The atomic notation is the same as in Figure 13.

Fe–Cu and for Cu–Cu interactions. The dimensions of the supercell are $13 \times 20 \times 3$ nm³, and the system consists of approximately 64,800 atoms. Interestingly, the interatomic potentials of Refs. [76, 88] give a non-polarized (symmetric) dislocation core for pure Fe and a fully-polarized (asymmetric) core for the three AR Cu precipitate, both in excellent agreement with our results using the IRP approach. We find that the Cu nano-cluster *enhances* substantially the edge component of the dislocation, as shown in Figure 14, suggesting that it may facilitate kink nucleation, which is in agreement with experiment.[91] However, three-dimensional simulations, currently under study, are necessary to confirm our conjecture of the Cu-induced facilitation of kink formation in Cu nano-precipitates of small diameters (<1 nm). The non-glide stress (Escaig stress) is defined as the edge component of the diagonal stress tensor interacting only with the edge component of the dislocation displacement field.[45, 92] Consequently, since the Cu nano-precipitate enhances the edge component, the non-glide shear stress will have a larger effect on the core structure and the cross-slip properties in Fe–Cu alloys, in contrast to pure Fe.

Next, using the FS atomistic potentials we examine the glide paths of the core for an applied pure glide shear stress on the $(1\bar{1}0)$ plane in the $\langle 111 \rangle$ direction. We increase the stress incrementally and relax the configuration between each increment. σ_P for pure Fe is 1.2 GPa and is well defined. Namely, below this critical stress the dislocation is stable, and above it the core moves.

In sharp contrast, there are two critical stresses for the Cu precipitate. The dislocation core structures for these two critical stress values of 0.8 GPa and 1.5 GPa, are shown in Figures 15(a) and (b), respectively. When the applied stress reaches 0.8 GPa, the dislocation moves by one atomic distance and exhibits a *split* core which is *metastable*. This metastable configuration remains fixed until the second upper critical stress of 1.5 GPa is reached, above which the motion becomes unbounded, i.e., the Cu cluster induces a *stable* $\rightarrow$ *metastable* $\rightarrow$ *stable* transition for the dislocation core under external stress. The IRP approach for the Fe–Cu system gives similar results as
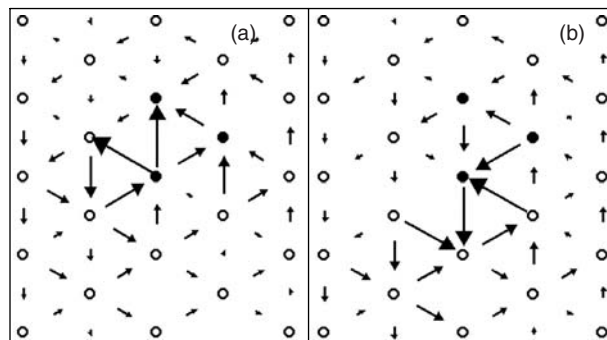
the atomistic simulations using the FS potential, but with different values of the critical stresses, listed in Table V. A similar behavior for the existence of two critical stresses was found[93] in pure Fe using the potential developed by Simonelli et al.[94] It is interesting to note that σ_P for pure Fe lies between the upper and lower values of the critical stress for the Cu precipitate, and the upper value agrees with a recent estimate.[83] This result indicates that the nano-cluster cylindrical Cu precipitate strengthens α-Fe. However, the strengthening mechanism is more complex, involving a two-step change of the dislocation mobility, with the Peierls stress of the second step being higher than that of pure Fe.

There are several available FS interatomic potentials for Fe–Cr.[95–102] Here we use that developed by Olsson[95] because of its compatibility with Ackland's potential for pure α-Fe.[76] The result shows that the critical shear stress to move the dislocation core on the {110} plane in the Fe–Cr system is also well defined and unique, but with the value of 2.0 GPa, which is 67% higher than that in pure α-Fe. For comparison, we also list in Table V the result of σ_P using the IRP method, which is consistent with the FS calculation. Thus, our results indicate that the SSH effect of Cr clusters is due to the fact that they serve as obstacles for dislocation motion, due to the strong bonding of Cr pairs or clusters, consistent with the interatomic results of Wallenius et al.[97]

3.4. γ-Precipitate Strengthening in Nickel-Based Superalloys

One of the interesting applications is the strengthening caused by precipitation in nickel-based superalloys.

Table V. Values of critical stress (σ_P) in GPa using the IRP methods and the FS potential, respectively. The lower and upper values of σ_P^l and σ_P^u for the Fe–Cu system are explained in the text.

	Pure Fe	Fe–Cu (σ_P^l)	Fe–Cu (σ_P^u)	Fe–Cr	Pure Cr	BCC Cu
IRP	1.6	1.3	1.9	1.8	2.1	1.8
FS	1.2	0.8	1.5	2.0	2.3	1.7

REVIEW

These alloys have been extensively investigated, because the L1$_2$-type long-range ordered intermetallic compounds, such as Ni$_3$Al, Ni$_3$Si and Co$_3$Ti, are considered for high-temperature structural applications. Miller observed extensive formation of spherical γ-precipitates in the γ' matrix phase of a nickel-based superalloy using 3-D atom probe measurements.[103] Nemoto et al. measured the increase in the yield strength of the alloy resulting from the formation of γ-precipitates, and provided a clear picture of the influence of γ-precipitate strengthening on the inverse temperature dependence of the yield strength of the alloy.[104] Thus, understanding the role of γ-precipitates on alloy strength, and the detailed mechanisms involved during the interaction between a dislocation and γ-precipitates is fundamental to the control and improvement of the mechanical properties. Using the hybrid atomistic-continuum method discussed earlier,[23, 105] the interaction between a super-dislocation and a spherical γ-precipitate embedded in a γ' matrix of a nickel-based superalloy was studied by Takahashi et al.[106] The focus of their study was on the investigation of two main effects: (1) the influence of the dislocation line flexibility, and (2) the effects of the dislocation core structure on precipitation strengthening. In the following, we show how the two methods are coupled to study the interaction between dislocations and precipitates.

3.4.1. Dislocation-Precipitate Elastic Interaction

Consider an infinite elastic body D, with elastic constants C_{ijkl}, containing N_p precipitates and N_d dislocations, subjected to an external applied stress σ_{ij}^0. The mth precipitate, Ω^m, has elastic constants C_{ijkl}^m, and induces a coherency strain ϵ_{kl}^m. Following Mura,[107] the stress in an infinite elastic body can be written as

$$\sigma_{ij}^0 + \sigma_{ij} = \begin{cases} C_{ijkl}(\varepsilon_{kl}^0 + \varepsilon_{kl}) & \text{in } D - \Omega \\ C_{ijkl}^m(\varepsilon_{kl}^0 + \varepsilon_{kl} - \epsilon_{kl}^m) & \text{in } \Omega^m \end{cases} \quad (27)$$

where, $\varepsilon_{kl} = C_{klij}^{-1}\sigma_{ij}^0$, and Ω is the total volume occupied by N_p precipitates. Since it is difficult to solve Eq. (27) directly, the superposition principle will be utilized in its solution

$$\sigma_{ij}^0 + \sigma_{ij} = \hat{\sigma}_{ij} + \tilde{\sigma}_{ij} \quad (28)$$

where $\hat{\sigma}_{ij}$ is the stress in the elastic problem containing dislocations with an external applied stress given by

$$\hat{\sigma}_{ij} = C_{ijkl}(\varepsilon_{kl}^0 + \hat{\varepsilon}_{kl}) \quad (29)$$

The last equation can be solved using the PDD method. On the other hand, $\tilde{\sigma}_{ij}$ is a correction stress to the infinite medium solution, which should have an exact solution presented by Eq. (27), when combined with Eq. (29). Therefore, $\tilde{\sigma}_{ij}$ can be defined as

$$\tilde{\sigma}_{ij} = \begin{cases} C_{ijkl}\tilde{\varepsilon}_{kl} & \text{in } D - \Omega \\ C_{ijkl}^m(\tilde{\varepsilon}_{kl} - \epsilon_{kl}^m) + (C_{ijkl}^m - C_{ijkl})(\varepsilon_{kl}^0 + \tilde{\varepsilon}_{kl}) & \text{in } \Omega^m \end{cases} \quad (30)$$

According to Eq. (30), the correction field can be obtained from the solution of an inhomogeneous inclusion problem, with an initial stress $(C_{ijkl}^m - C_{ijkl})(\varepsilon_{kl}^0 + \tilde{\varepsilon}_{kl})$ in the precipitates. Takahashi and Ghoniem derived boundary and volume integral equations for such an inhomogeneity problem (Eq. (30)), which were solved using the the BEM method with a volume integral term. In the nickel-based superalloy γ-precipitate case, the elastic constants of both γ' and γ-phase are nearly the same, and thus the initial stress can be assumed to be zero. Thus, Eq. (30) can be converted from the inhomogeneous inclusion problem to an inclusion problem. Additionally, if the shape of the precipitate is assumed to be an ellipsoid, the equation can be solved using the Eshelby tensor instead of the BEM method, which will drastically decrease the computational effort.[108]

3.4.2. Elastic Field of Incoherent Spherical γ-Precipitates

Since experimental observations suggest that most γ-precipitates in Ni-based superalloys have spherical or cuboidal shapes, we assume that the shape of the γ-precipitate is spherical, and utilize an analytical solution to the elastic field generated by the γ-precipitate.[108] The lattice constants of the γ-precipitate and the γ'-phase are $a_0^\gamma = 0.352$ nm and $a_0^{\gamma'} = 0.357$ nm, respectively. This small lattice constant mismatch introduces a coherency strain $\in$

$$\in = (a_0^\gamma - a_0^{\gamma'})/a_0^{\gamma'} \quad (31)$$

in the γ-precipitate of -0.0143. When the position of interest is inside the inclusion, the analytical solution to an elastic problem of a spherical inclusion with a coherency strain $\in$ is given by

$$\epsilon_r = \epsilon_t = \frac{1+\nu}{3(1-\nu)} \in \quad (32)$$

where ν is Poisson's ratio, and ϵ_r and ϵ_t are the strain in the radial and tangential directions, respectively. On the other hand, when the point of interest is outside the inclusion, the strains are given by

$$\epsilon_r = -\frac{2}{3}\frac{1+\nu}{1-\nu}\frac{a^3}{r^3} \in$$
$$\epsilon_t = \frac{1}{3}\frac{1+\nu}{1-\nu}\frac{a^3}{r^3} \in \quad (33)$$

where, a is the radius of the spherical inclusion, and r is the distance between the center of inclusion and the point of interest. The stress tensor at the point can then be easily calculated using Hooke's law, once the strain tensor is available.

Figure 16 shows the simulation volume used in this work. The matrix material of the simulation volume is the γ'-phase, and the x, y and z axes are along the crystal orientations $[\bar{1}01]$, $[111]$, $[\bar{1}2\bar{1}]$, respectively. A straight edge

REVIEW
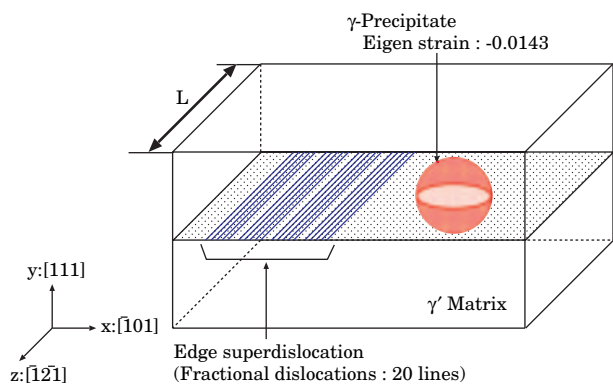
Fig. 16. Schematic of simulation model for PDD simulations.

super-dislocation is introduced into the simulation volume. The super-dislocation has a Burgers vector of $a_0^{\gamma'}[\bar{1}01]$, and is on the (111) slip plane, where a_0 is the lattice constant of the $L1_2$ ordered lattice nickel-aluminum (0.3571 nm).[109] The core structure of the super-dislocation is represented with 20 fractional dislocations. The GSFSs of the γ'-phase and of the γ-precipitate are calculated using the inter-atomic potential developed for the nickel-aluminum binary system.[109] The lattice restoring stresses are then calculated by taking the derivative of the GSFS, and are used as a function of position of the fractional dislocations. When a fractional dislocation is in the γ'-phase it experiences the lattice restoring stress of the γ'-phase, whereas when it is in the γ-precipitate it experiences the lattice restoring stress for of the γ-precipitate. In reality, the GSFS of the interface between the γ and γ'-phase is generally different from both the γ-surface of the γ and γ'-phases. However, for simplicity, the unique shape of the γ-surface at the interface is ignored. A spherical γ-precipitate with a coherency strain of $\in = -0.0143$ is placed at the front of the super-dislocation. Periodic boundary conditions are applied in the z-direction, assuming that the dislocation is infinitely long, yielding a 1-D periodic array of precipitates in this direction. To move the dislocation, an external shear stress, τ_{xy}, is applied to the volume, and is controlled to measure the CRSS for the interaction. The two important parameters controlling the CRSS are the size of the simulation volume along z, L, and the diameter of the precipitate, D.

Figure 17(b) shows the calculated GSFS for the γ'-phase, where an anti-phase boundary (APB) forms behind a leading dislocation, and a trailing dislocation terminates the APB. Thus, dislocations must move in pairs in a *super-dislocation* configuration. In the present calculation of the GSFS for the γ'-phase, the maximum displacement is $40\Delta u$, which is twice of that given to the atomic volume in the GSFS calculation of the γ-phase. The two local maxima in the GSFS lead to the formation of an extended dislocation in the super-dislocation core. Moreover, the two local minima at $u = 0.42b$ and $1.0b$, correspond to the complex stacking-fault between
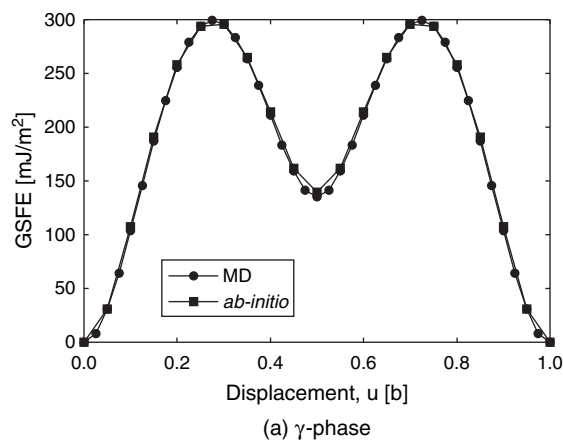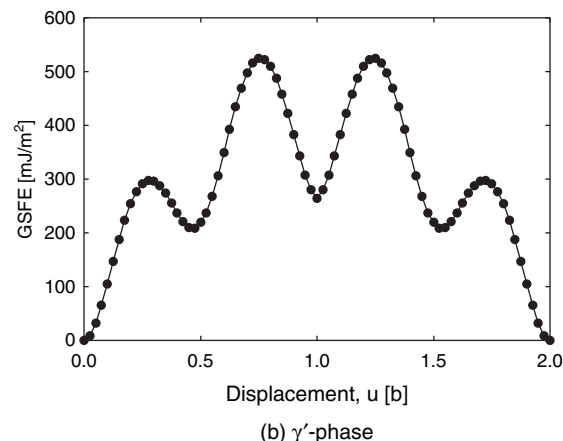
Fig. 17. Generalized stacking-fault surface energy for the γ (a) and γ' (b) phases.

the two partial dislocations of the extended dislocation, and the APB between two super-partials of the super-dislocation. The complex stacking-fault and APB energies are 202 mJ/m² and 252 mJ/m²,[109] compared to the experimental values of 235 mJ/m² and 175 mJ/m²,[110] respectively.

3.4.3. γ-Precipitate Strengthening

γ-precipitate strengthening in nickel-based superalloys is a result of several mechanisms that operate concurrently. Following Ardell,[111] the chemical strengthening and modulus hardening do not substantially affect the overall strength of the alloy. Gerold and Haberkorn developed an analytical solution to the increase in the CRSS as a result of coherency interaction between a dislocation and a precipitate.[112] To obtain a closed form solution, they assumed that the dislocation shape is straight, and that the dislocation core is infinitely narrow (i.e., the displacement field has a discontinuity at the line). Let us now consider an edge dislocation on the x–y slip plane located at z_0 and gliding in the x direction, together with a precipitate of radius R and a coherency strain $\in$. When the dislocation line is at a position (x, z_0), it suffers an interaction force $K(x)$ from the precipitate,

J. Comput. Theor. Nanosci. 7, 1–30, **2010**

19

which can be calculated by integrating the Peach-Koehler produced by the precipitate along the dislocation line (y direction), and is given by

$$K(x) = b\int_{-\infty}^{\infty} \tau_{xz}(x, y, z_0)dy = \frac{8}{3}\frac{1+\nu}{1-\nu}\frac{Gb| \in |R^3 x_0 z_0}{(x_0^2 + z_0^2)^2}$$

$$\times \left\{ 1 - \frac{y_0(2R^2 + x^2 + z_0^2)}{2R^3} \right\} \qquad (34)$$

where

$$y_0^2 = \begin{cases} R^2 - (x^2 + z_0^2) & (x^2 + z_0^2 < R^2) \\ 0 & (x^2 + z_0^2 \geq R^2) \end{cases}$$

The CRSS can be calculated from the maximum interaction force

$$\tau_{\text{crss}} = \frac{K(x)|_{\text{max}}}{bL} \qquad (35)$$

In order to investigate the influence of coherency strengthening alone, we use the GSFS for the γ'-phase for both the matrix and precipitate. The diameter of the γ-precipitate is fixed to 8 nm, and the position of the slip plane is 3 nm above (below) the precipitate's mid-plane, corresponding to the precipitate being in the compression (tension) side of the dislocation, shown in Figures 18(a and b). The size of the simulation volume is taken as $50 \times 50 \times 20$ nm^3. Figure 18 shows successive snap-shots of the dislocation geometry during its interaction with the γ-precipitate. Note that each line represents a constant displacement contour within the dislocation core, with values in the range (0,b). The fractional dislocations (each representing a constant displacement contour) cluster into four groups, corresponding to the leading and trailing partials of the super-partials of the super-dislocation, respectively. In Figure 18(a), where the slip plane is 3 nm above the mid-plane, the central part of the dislocation is immobilized by the coherency strain at the front of the precipitate. In this case, most of the precipitate is on the compression side of the super-dislocation, and the precipitate has a negative coherency strain. Therefore, the super-dislocation and the precipitate have a repulsive interaction force. Upon increasing the applied shear stress, the leading super-partial starts to cut through the precipitate. Once the dislocation moves inside the precipitate, it is strongly pushed to the outside of the precipitate by the interaction. After breaking away from the precipitate, the super-dislocation is still influenced by a repulsive interaction force that enhances its glide. On the other hand, as shown in Figure 18(b), the central part of the super-dislocation spontaneously dissociates inside the precipitate, because most of the precipitate is on the tension side of the dislocation and the precipitate has an attractive interaction force with the super-dislocation. Thus, the super-dislocation tends to stay inside the precipitate so that the maximum interaction appears at the center of the precipitate. When the applied shear stress reaches the CRSS, the dislocation can finally cut through the precipitate.

These results will now be utilized to extend the applicability of Eq. (35) by incorporating the influence of the core structure of dislocations as they interact with the precipitates. We decompose here the super-dislocation into four

(a)

(b)
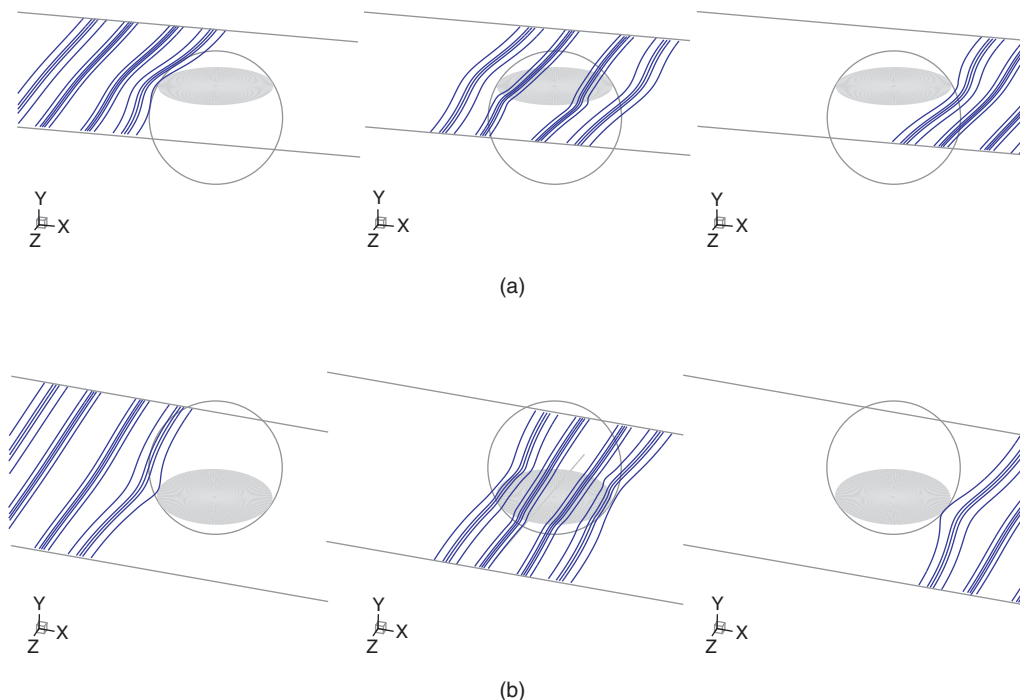
Fig. 18. Snapshots of the dislocation core structure during the interaction between a super-dislocation and a γ-precipitate accounting only for precipitate coherency strain. (a) Slip plane position: 3 nm above the precipitate's mid-plane. (b) Slip plane position: 3 nm below the precipitate's mid-plane
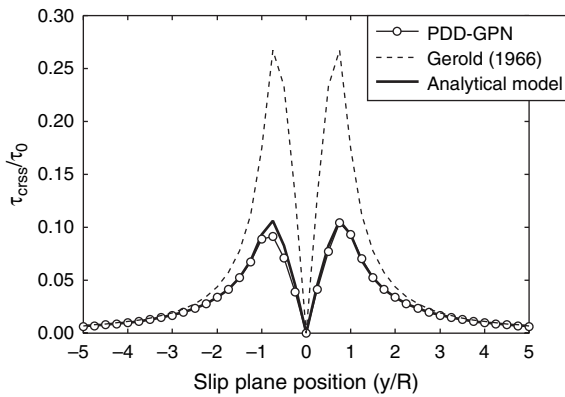
Fig. 19. Increase in CRSS as a function of the slip plane position as a result of the coherency strengthening by the precipitate strain field, calculated by direct numerical simulations, and compared to the results of Gerold and the proposed analytical model.

partial dislocations D_i, where the positions of each partial dislocation x_i is assumed to be $x_2 = x_1 + w_c$, $x_3 = x_2 + w_a$ and $x_4 = x_3 + w_c$, where w_c and w_a are the widths of the complex stacking-fault between two partial dislocations of a super-partial dislocation, and the anti-phase boundary between the super-partial dislocations. For simplicity, we consider an infinitely long straight edge super-dislocation in an infinite isotropic elastic body, and include the elastic interaction between the partial dislocations as well as the energy of the complex stacking-fault and anti-phase boundaries. The widths w_c and w_a can be calculated by solving the following equilibrium equations,

$$\frac{Gb^{e2}}{2\pi(1-\nu)}\left(\frac{1}{w_c} + \frac{1}{w_c+w_a} + \frac{1}{2w_c+w_a}\right)$$
$$+ \frac{Gb^{s2}}{2\pi}\left(-\frac{1}{w_c} + \frac{1}{w_c+w_a} - \frac{1}{2w_c+w_a}\right) = \gamma_c \quad (36)$$

$$\frac{Gb^{e2}}{2\pi(1-\nu)}\left(-\frac{1}{w_c} + \frac{1}{w_a} + \frac{1}{w_c+w_a}\right)$$
$$+ \frac{Gb^{s2}}{2\pi}\left(\frac{1}{w_c} - \frac{1}{w_a} + \frac{1}{w_c+w_a}\right) = \gamma_a - \gamma_c \quad (37)$$

In analogy with Eq. (35), the CRSS corresponds to the maximum value of the sum of the $K(x_i)$, $(i = 1–4)$,

namely,

$$\tau_{crss} = \frac{\sum_i^4 K(x_i)|_{\max}}{bL} \quad (38)$$

Figure 19 shows the results of the PDD with the GPN model simulation, which are compared to calculations based on Eq. (35) as well as Eq. (38). The increase in CRSS calculated by Eq. (38) is considerably smaller than those calculated by Eq. (35), which is in excellent agreement with the numerical simulation results. Thus, it is clear that the influence of the core structure of dislocations on coherency strengthening is very significant (the maximum is lowered by a factor of almost three), and that the influence can be accurately accounted for using the proposed Eq. (38).

If the energy of the stacking fault between two partial dislocations is larger inside the precipitate than in the matrix, an additional shear stress must be applied on the dislocation to overcome that energy difference, $\Delta\gamma$, and allow the dislocation to cut through the precipitate. Nembach derived an analytical expression to calculate the required shear stress due to stacking-fault strengthening.[113] An extended dislocation, composed of two partial dislocations and a stacking-fault in-between were considered, and the length of each partial dislocations inside the precipitate, $L(x)$ was used to find the interaction force between the precipitate and the dislocation K

$$K(x) = (L(x) - L(x+w))\Delta\gamma \quad (39)$$

where, $L(x)$ and $L(x+w)$ are the lengths of the leading and trailing partial dislocations, at x and $x+w$, inside the precipitate, respectively. The CRSS can be calculated by finding the maximum interaction force, given by:[113]

$$\tau_{crss} = \frac{K(x)|_{\max}}{bL} \quad (40)$$

To determine the accuracy of the analytical solution of Nembach, and the effect of the exact core structure on the stacking fault strengthening, we have performed numerical simulations where the influence of the coherency strain is removed by setting $\epsilon = 0$. The simulation volume used here is identical to that used in the previous section, and the diameter of the precipitate is changed in the range from 2 to 30 nm. The slip plane position of the super-dislocation is fixed at the center of the precipitate. Figure 20

REVIEW
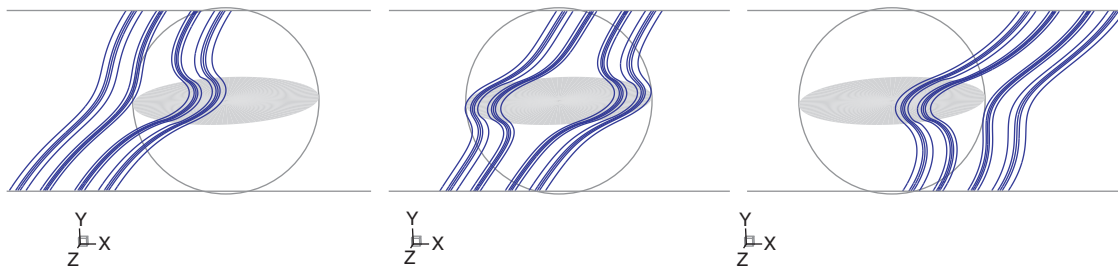
Fig. 20. Snapshots of the interaction between a super-dislocation and a 16 nm-γ-precipitate as a result of differences in the stacking fault between the matrix and precipitate (stacking fault strengthening).

shows snapshots of the dislocation configuration as it interacts with a 16 nm-precipitate. It is clear that the super-dislocation and the precipitate are attracted to one another, and that the super-dislocation is first absorbed by the precipitate. When the dislocation enters the γ-precipitate, the anti-phase boundary disappears, and the complex stacking fault is changed to an intrinsic stacking-fault, which has a lower energy than the complex stacking-fault. Thus, the super-dislocation tends to be attracted inside the precipitate to reduce the interaction energy. Increasing the external shear stress, the dislocation gradually starts to bow-out, and finally breaks away from the precipitate when the applied shear stress reaches its CRSS value.

Figure 21 shows the results of the numerical simulations using the full PDD-GPN model and the rigid PDD-GPN model. Also, the results of Eq. (40) are plotted for comparison. The CRSS increases as the precipitate diameter increases, which is a consequence of an increase in the stacking fault area between the partials entering the precipitate. The results of all numerical simulations with both methods and those of Eq. (40) are within a few percent. Therefore, Eq. (40) reasonably accounts for the stacking fault strengthening, as long as the dislocation core can be described by two isolated peaks of displacement distributions (i.e., well-isolated partials). This clearly demonstrates that the core structure of the dislocations is an important factor in determining the CRSS, and that Eq. (40) can be used in cases where the two partial dislocations are well-isolated.

Following the work of Takahashi and Ghoniem,[106] we describe here the γ-precipitate strengthening as a combination of stacking-fault and coherency strengthening effects, and propose a method to evaluate the overall CRSS increase when the two mechanisms operate simultaneously. The simulation volume and boundary conditions used here are the same as those used in previous simulations, while the diameter of the γ-precipitate is fixed to 8 nm. Figure 22 shows the dependence of the CRSS on the location of the slip plane. As can be seen, in the stacking-fault
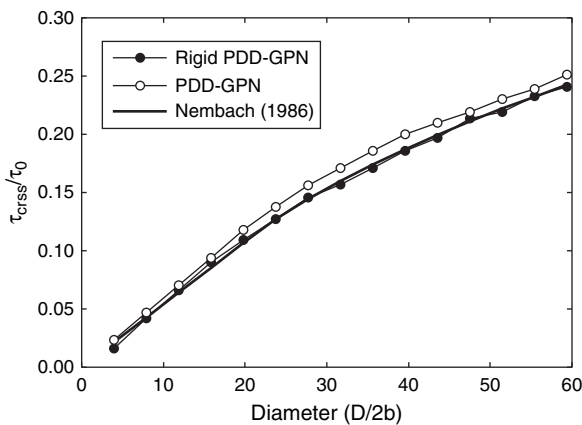
strengthening mechanism, the distribution of CRSS is symmetric about the precipitate center, exhibiting a maximum at the center. When the position of the slip plane is outside the precipitate, there is no increase in CRSS, as expected. It is clear that the CRSS outside the precipitate is identical to that due to the coherency strain mechanism, while inside the precipitate both the coherency and stacking fault mechanisms operate simultaneously. In fact, as the slip plane gets closer to the precipitate mid-plane, the influence of coherency strain diminishes, while stacking fault strengthening reaches its maximum. However, the distribution of the CRSS when the two mechanisms operate simultaneously (mixed strengthening) has a complex structure as a function of the slip plane position, and its maximum cannot be simply the sum of the two independent maxima for each mechanism separately; a procedure that is common in precipitation hardening estimates. To further demonstrate this point, we have also used a simple summation rule for the CRSS resulting from the stacking-fault and the coherency strengthening mechanisms, and plotted the result in Figure 22 (dashed line). Here, the simple sum does not represent overall precipitate hardening very well. When the dislocation is on the compression side of the precipitate, the stacking fault shrinks, while it widens when it is on the tension side, giving rise to the asymmetric distribution of the CRSS as a function of the slip plane position, when the two mechanisms operate simultaneously; a result that cannot be predicted by simple addition of the two effects.

Using Eqs. (38) and (40), the interaction forces between the super-dislocation and the precipitate are plotted in Figure 23 as a function of dislocation position from the precipitate center, when the slip plane is at -2.0 nm below the precipitate's mid-plane. It is observed that the peaks of the interaction force due to the stacking-fault and the coherency mechanisms appear at different positions, suggesting that the summation of the CRSS (which is equivalent to summing the maximum forces) is not a good way to represent the true spatial dependence of the

Fig. 21. Dependence of the CRSS on precipitate diameter for the stacking-fault strengthening mechanism alone.
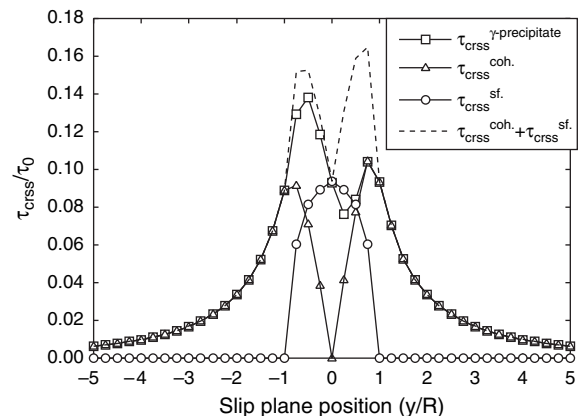
Fig. 22. CRSS as a function of the slip plane position for coherency (triangles) and stacking fault (open circles) mechanisms, simple summation (dashed line), and full calculation (open squares).

22

J. Comput. Theor. Nanosci. 7, 1–30, **2010**
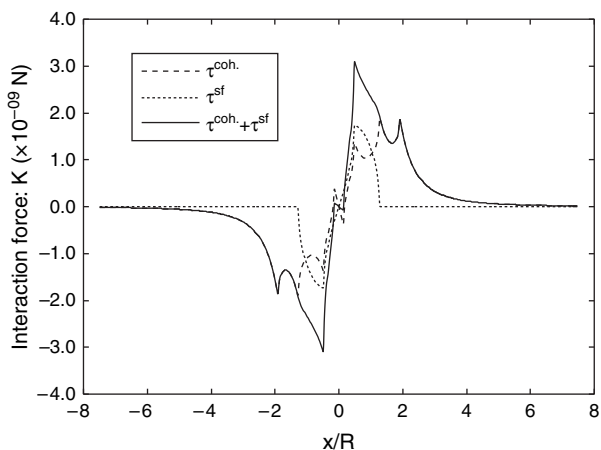
Fig. 23. Dependence of the coherency and stacking fault interaction forces on the dislocation position, when it lies on a slip plane at -2 nm below the precipitate's mid-plane.

CRSS for the mixed strengthening. The figure also shows the total interaction force due to the stacking-fault and coherency strengthening mechanisms as a function of dislocation position. Since the dislocation has to overcome the maximum total interaction force, we have calculated the CRSS at different slip planes using only the maximum interaction force. In Figure 24 we compare the CRSS as a function of the slip plane position, using the full PDD-GPN model, and comparing it to the more simplified model of using only the maximum value of the calculated shear stress at each slip plane. These two methods show excellent agreement, indicating that, in order to calculate the CRSS for mixed strengthening, the maximum interaction force for a given slip plane can be first computed and stored, and then used in subsequent DD simulations without having to perform detailed simulations.

3.5. Dislocation Transmission Across Cu/Ni Interface

The influence of interfaces on the mechanical properties of multiphase and polycrystalline materials is ubiquitous. It
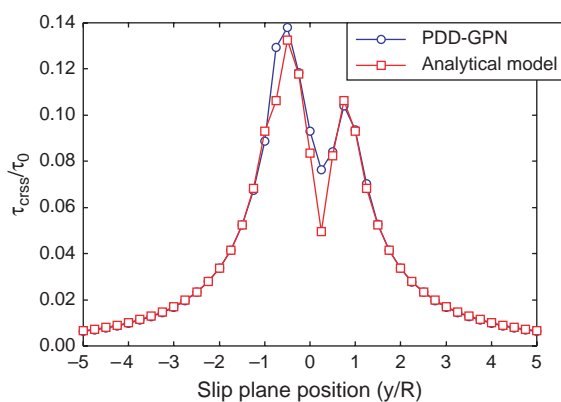
Fig. 24. Comparison of the CRSS using the full PDD-GPN model with the analytical model as a function of slip plane position.

has been found experimentally that the hardness and ultimate tensile strength of nano-layered structures increases with decreasing bilayer thickness, in a relation analogous to the Hall-Petch behavior to some critical layer thickness. At smaller wavelengths, the hardness is seen to increase more rapidly, with Hall-Petch exponents of the order of unity or greater, to some peak stress value that is much greater than that attainable by traditional microstructures. Thus, multilayers composed of alternating layers made of metals such as Cu, Ni, Cr and Nb exhibit peak strengths on the order of few GPa at layer thickness of few nanometers[114, 115] compared to the yield strength values of few tens of MPa in bulk Cu, Ni, Cr and Nb.

A pronounced size effect has been observed in thin multilayers systems as different deformation mechanisms operate at different length scales. While the behavior of multilayers can be described by scaling law in the submicron length scale, deviation from this scaling law occurs at the nanoscale, and the effect of discrete or even single dislocation strengthening mechanism applies.[19] At the nanoscale, the strengthening mechanisms fall into several broad categories. The first mechanism is the classic Hall-Petch model of dislocation pileups.[17, 18, 116] The second mechanism was introduced by Koehler,[117] where the image forces imposed by the layers of alternating materials restrict the motion of dislocations.[118] The dislocations are attracted toward (repelled from) the interface by the decrease (increase) in line energy as a dislocation moves toward the material with lower (higher) elastic constants. Another deformation mechanism involves the formation and propagation of the so-called "Orowan" bows within the layer.[119]

3.5.1. Generalized Stacking Fault Energy Surface

The Cu/Ni bi-material system is modeled as two semi-infinite homogenous and isotropic regions connected at the interface as shown in Figure 4(c). The glide planes of Cu and Ni are assumed to be coplanar and normal to the interface. A pure screw dislocation of Burgers vector is placed in Cu (soft material) gliding on the (111) plane. The electronic structure calculations of the GSFS were carried out using the projector augmented-wave (PAW) method[120] as implemented in the VASP code.[47, 121] The *ab initio*-determined GSFS projected along the[121] direction for the pure Cu and Ni and along the [001] direction for the Cu/Ni interface are shown in Figure 25. The first energy maximum encountered along the[121] direction for the Cu and Ni is the unstable stacking fault energy, γ_{uns}, which represents the lowest energy barrier to nucleate a dislocation from a crack tip at 0 K. At finite temperatures, the effective energy barrier for dislocation nucleation will be reduced by both thermal excitations and the fact that dislocation nucleus may take a three-dimensional shape. The local minimum on the other hand, corresponds to the intrinsic
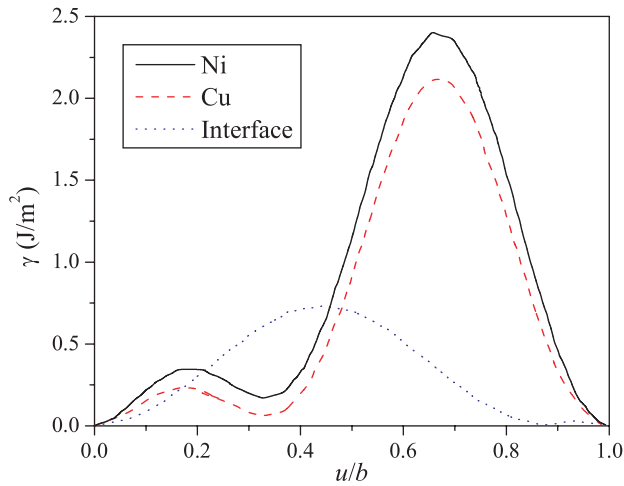
Fig. 25. *Ab initio* generalized stacking fault energy for Ni and Cu along the [112] direction and for the Cu–Ni interface along the [100] direction.

stacking fault energies, γ_{ins}. The calculated values of γ_{uns} are 225 mJ/m^2 and 350 mJ/m^2 for Cu and Ni, respectively, while the values of γ_{int} for Cu and Ni are 53 mJ/m^2 and 163 mJ/m^2, respectively. These values are in good agreement with other calculations.[122] As expected, the GSFS of the interface is symmetric along the[110] direction and it has unstable stacking fault energy of 730 mJ/m^2, which is much higher than the corresponding value of Ni and Cu. The absence of a saddle point in the GSFS of the interfaces suggests that the full dislocation on the interface does not dissociate. The shear modulus, Burgers vectors, and the values for the various stacking fault energies for Ni and Cu are listed in Table VI.

3.5.2. Displacement and Density Profiles

The large increase in the mechanical strength of nano-layered materials is widely attributed to the presence of interfaces. Several factors can affect the mechanical and physical properties of the interface such as: the unstable stacking fault energy of the interface, γ_{int}, which is a measure of the propensity of interfacial sliding and which is directly related to the electron charge bonding across the interface, the presence of misfit dislocations, and the presence of impurities. The smaller γ_{int} is, the easier is for the interface to slide, thus allowing the dislocation to spread onto the interface.

Table VI. Values of the shear modulus, μ, the Burgers vector b, the intrinsic and unstable stacking fault energies, γ_{int} and γ_{uns}, and the drag coefficient, B in the dislocation dynamics, for Ni and Cu, respectively.

Material	μ (GPa)	b (Å)	γ_{int} (mJ/m^2)	γ_{uns} (mJ/m^2)	B (Ns/m)
Ni	80	2.5	163	225	10^4
Cu	50	2.6	53	350	10^4

Figure 26 shows the equilibrium edge and screw displacement and the corresponding Burgers vector density $\rho(x)$ of the dislocation for three values of applied stress. The edge and screw Burgers vector density are defined by $\rho^e = du^e(x)/dx$ and $\rho^s = du^s(x)/dx$. The screw dislocation, originally placed in the soft material ($x > 0$) is pushed towards the Cu/Ni interface. For relatively low values of applied stress (around 2.0 GPa), the dislocation core in Cu dissociates into two partials bounding a stacking fault with a separation distance of about $7b$, as shown in the top panel of Figure 26. As the external stress increases, the dislocation approaches the interface but remains dissociated. However, the dislocation core structure has changed significantly. First, the dislocation Burgers vector density
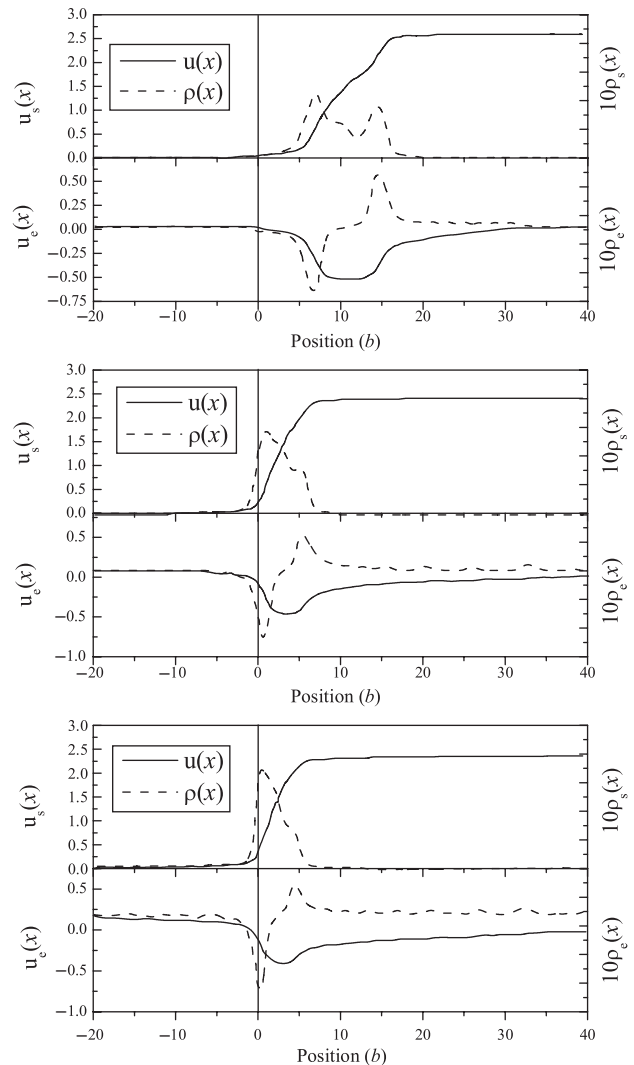
Fig. 26. Displacement, $u(x)$, and density, $\rho(x)$, profiles on the glide plane for the edge and screw components, respectively, as it moves from Cu towards Ni. The GSFS of the interface is equal to the *ab initio* value ($\gamma_{int} = \gamma_{int}^{ab}$). The profiles show the equilibrium positions of the dislocation at (2.0 GPa (top panel), 2.8 GPa (middle panel) and 3.30 GPa (bottom panel). The continuous lines represent the screw or the edge displacements, respectively, and the dotted lines represent the corresponding densities.

accumulates on the leading partial at the expense of the trailing partial, as shown in the middle and bottom panels of Figure 26, respectively. Second, the dislocation core constricts steadily and there is a significant overlap between the two partials (bottom panel of Fig. 26). Note, that the maximum value of the screw component of the displacement in Cu is 2.35 Å, while the Burgers vector of Cu is 2.6 Å. This reduction of Burgers vector is a result of the energetically favorable spreading of the core onto the interface. Our results suggest that the dislocation spreading process proceeds via the following mechanism: When the leading fractional dislocation reaches the vicinity of the interface it spreads on it, if it is energetically favorable. As the external stress is increased, the trailing fractional dislocations follow and spread onto the interface. The spreading process continues until the interface can no longer accommodate additional slip. At the critical value of the applied stress, once the leading dislocation on the glide plane overcomes the interfacial barrier and is transmitted to the Ni crystal, the remaining fractional dislocations follow.

In Figure 27 we show the snapshots of the Burgers vector density profiles $\rho^e(x)$ and $\rho^s(x)$ of the dislocation under the critical stress value of 3.35 GPa. At the initial stage of the transmission process, most of the fractional dislocations are localized in the vicinity of the interface in the Cu host (Fig. 27(a)). As the fractional dislocations relax, they get transmitted through the interface towards the Ni host till all of them pass. Note, that after the dislocation has been transmitted, the density profile exhibits the formation of two partials with a separation distance of about $6b$ (Fig. 27(b)). The peak in the density profile at $x = 0$ indicates the formation of a ledge on the interface, in agreement with MD simulations for edge or mixed dislocations for the Cu/Ni interface.[55]
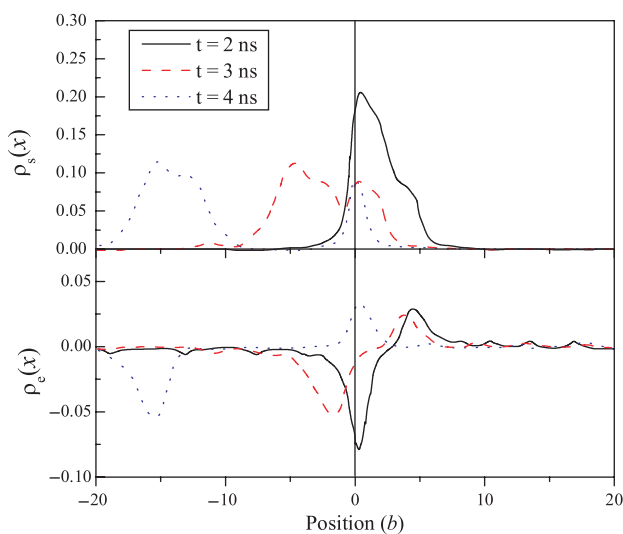
Fig. 27. Dynamic evolution of the dislocation density of the edge and screw components along the glide direction during the transmission process under the critical stress of 3.35 GPa. Positive (negative) position denotes the Cu (Ni) matrix.

3.5.3. Effect of Unstable Stacking Fault of the Interface

Interfaces can be coherent, semi-coherent or fully non-coherent. In the case of fully non-coherent structures, dislocation motion is restricted to individual layer,[118] i.e., the interface acts as a dislocation sink. For a semi-coherent interface as in the case of Cu/Ni, the dislocation transmission across the interface is possible depending on the stacking fault energy of the interface. In order to explore the effect of interfacial sliding on the critical stress required for dislocation transmission, we have varied the value of γ_{int} with respect to its *ab initio* value $\gamma_{int}^{ab} = 730$ mJ/m^2.

Figure 28 displays the dislocation displacement profiles for the screw component on the glide plane, $u^s(x)$, and on the interface plane, $u^s(y)$, for different values of the ratio, $\gamma_{int}/\gamma_{int}^{ab}$, of 1.2 (hard interface), 1.0, and 0.8 (soft interface). In each panel we show also the results for the displacement profiles for various applied stress. As expected, as the interfacial energy barrier for sliding is reduced and the interface becomes less bonded, the percentage of the dislocation spreading on the interface increases from about 13% for $\gamma_{int} = 1.2\gamma_{int}^{ab}$ to 30% for $\gamma_{int} = 0.8\gamma_{int}^{ab}$. The spreading of fractional dislocations on the interface imposes an extra energy barrier on the transmission of the glide dislocations. The extra barrier is due to the repulsive elastic interactions between the glide and interfacial fractional dislocations and the formation of the interfacial ledge which hinders the transmission process from Cu to Ni. Consequently, the critical value of applied stress for dislocation transmission increases (decreases) to the value of 4.2 GPa (3.2 GPa) as the interfacial GSFS decreases (increases) compared to its corresponding *ab initio* value. The ledge formation is partially due to the accommodation of the misfit in Burgers vector between Cu and Ni which is about 0.10 Å. A closer examination of Figure 27(b) however, shows that the screw displacement profile as the dislocation transmits from Cu to Ni has a step at the interface whose height is 0.25 Å, which is larger than the lattice constant mismatch of 0.1 Å.

3.5.4. Effect of Dislocation Splitting

Previous PN-based simulations[63–65] did not take into consideration the development of the edge component of a pure screw dislocation upon dissociation. This possibility results in dislocation splitting into a partial with mixed Burgers vectors, with an overall reduction of the energy, as compared to dissociation along screw components alone, which renders the dislocation with higher misfit energy. In order to explore the effect of the dislocation splitting on the spreading process, we have carried out several simulations in which we disallow the dislocation to split by considering the screw displacement only (i.e., removing the edge component associated with each screw dislocation).

*J. Comput. Theor. Nanosci. 7, 1–30, **2010***

25

REVIEW
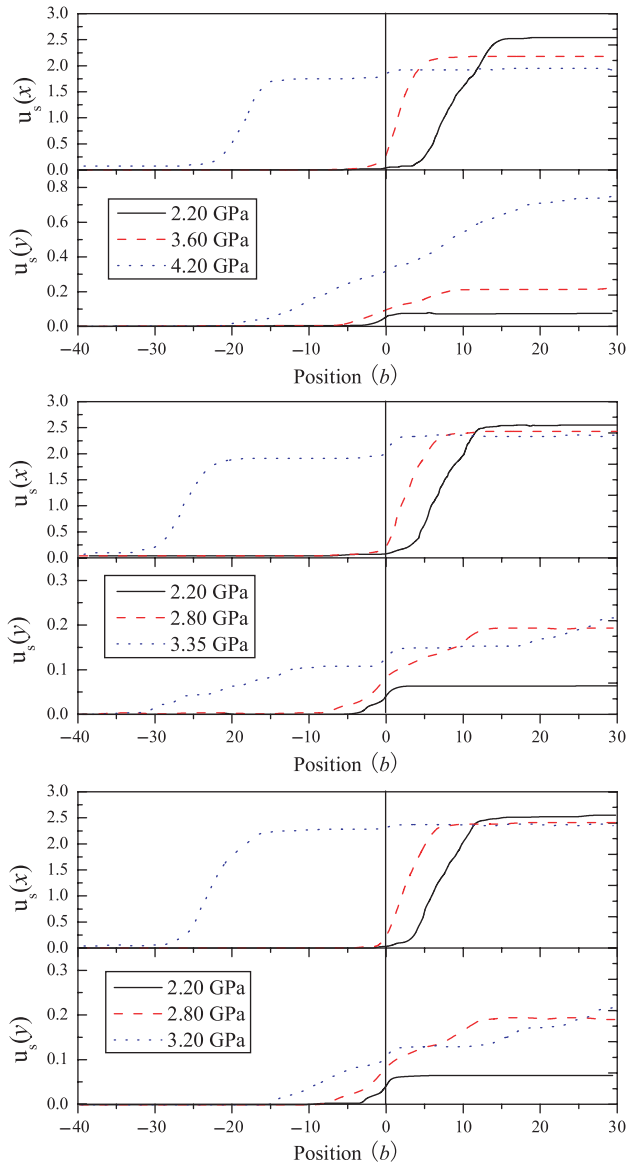
Fig. 28. Equilibrium displacement profiles of the screw component along the glide direction, $u^s(x)$, and on the interface plane, $u^s(y)$, for different values of $\gamma_{int}/\gamma_{int}^{ab}$ of (a) 0.8 (top panel), (b) 1.0 (middle panel) and (c) 1.2 (bottom panel), respectively. The solid, dashed, and dotted curves correspond to different values of applied stress.

The results are then compared with our previous results in Figures 26–28, where the edge component was taken into account explicitly.

Figure 29 shows the screw displacement, $u^s(x)$, and density, $\rho^s(x)$, profiles on the glide plane, and the screw displacement, $u^s(y)$, on the interfacial plane with and without the edge components. The removal of the edge components changes the dislocation core structure considerably. First, the dislocation core does not dissociate. Second, the dislocation core becomes much narrower, as reflected on the dramatic increase in the magnitude of the Burgers vector density. Finally, more dislocation core spreading onto the interface takes place, which in turns leads to a
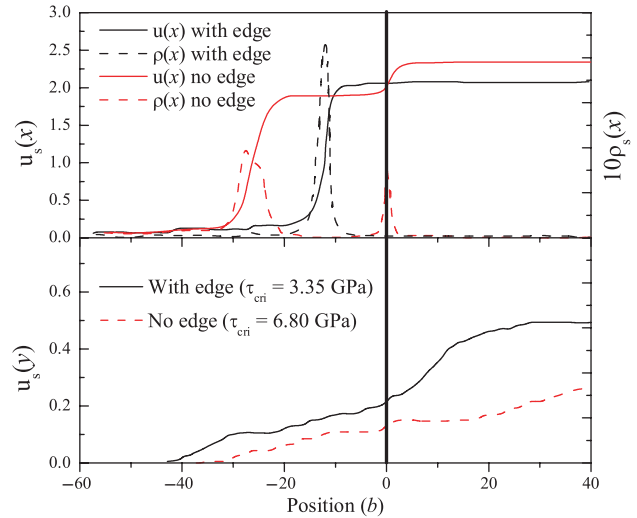
Fig. 29. Displacement, $u^s(x)$, and density, $\rho^s(x)$, profiles of the screw component on the glide plane and screw displacement, $u^s(y)$, on the interfacial plane for a screw dislocation with and without the associated edge component. The critical stress, τ_{crit}, for transmission is 6.80 (3.35) GPa without (with) the edge component.

significant increase in the transmission stress. By removing the edge components, the critical stress is doubled compared to the case where the edge component is taken into account explicitly. These results suggest that a constricted dislocation core can spread onto the interface much easier, which is analogous to the cross slip mechanism.[60]

3.5.5. Effect of Preexisting Misfit Dislocations

Interfacial misfit dislocations, interacting with the applied stress and incoming glide dislocations can be a potent barrier to slip transmission.[54] In this section we explore the effect of pre-existing misfit dislocations on the dislocation core properties and on the transmission stress. Two simulations were carried out in the absence or presence of preexisting misfit dislocation.

In the absence of a misfit dislocation, initially, the interface has zero displacement content and a single dislocation is placed on the slip plane having a maximum displacement of 2.6 Å. After the dislocation transmits from Cu to Ni as shown in Figure 30, it leaves part of its displacement on the interface. Therefore, the original displacement on the glide plane is reduced from 2.6 Å to 2.35 Å, whereas that on the interface is increased from 0 to 0.25 Å.

In the presence of a preexisting misfit dislocation, initially, we consider both a glide and a misfit dislocation on the slip and interfacial planes, respectively. The maximum displacement contents on both the glide and interface plane are equal to 2.6 Å. The fractional dislocations on the interface are allowed to interact with the glide fractional dislocations, where the glide fractional dislocations are allowed to spread on the interfacial plane and vice versa. After the dislocation transmission, as shown in Figure 30, the
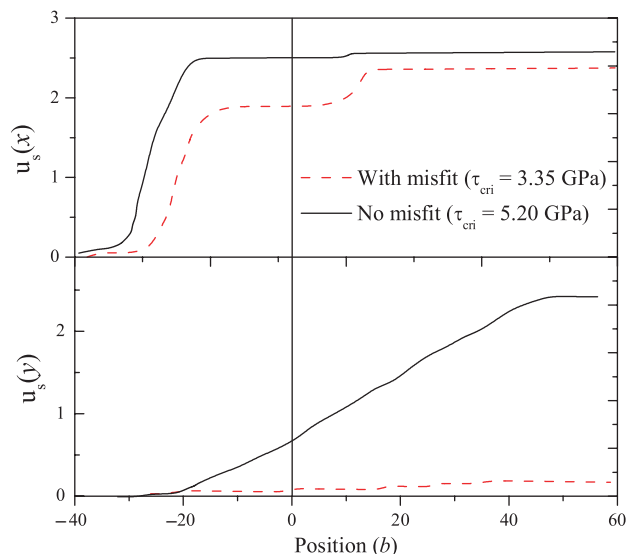
Fig. 30. Effect of pre-existing misfit interfacial dislocation on the displacement profiles of a screw dislocation in the presence and absence of pre-existing misfit dislocation. The displacement, $u^s(x)$, $(u^s(y))$ profile on the glide (interfacial) plane "after dislocation transmission" are shown on the top (bottom) panel.

displacement content on the glide and interfacial planes do not change from their initial values, indicating that the presence of a preexisting dislocation prevents any spreading from or to the glide plane.

The screw displacement, $u^s(x)$ $(u^s(y))$ profile on the glide (interfacial) plane, after the dislocation transmission, are shown in the top (bottom) panel of Figure 30, in the absence or presence of misfit interfacial dislocation. The results indicate that the transmission stress increases
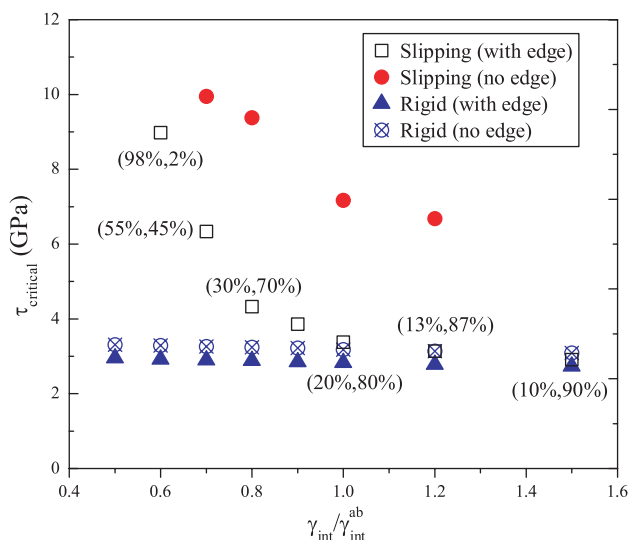
Fig. 31. Variation of critical shear stress with $\gamma_{int}/\gamma_{int}^{ab}$ of the interface. Rigid interface does not accommodate core spreading and therefore it is not affected by the change in the interfacial GSFS. The removal of the edge component leads to a significant increase in the transmission stress for the slipping interface case and minor increase for the rigid interface case.

dramatically compared to its corresponding value in the absence of the misfit dislocation. Note, that there is no ledge formation on the interface when the misfit dislocation is present.

Figure 31 shows the critical transmission stress versus the ratio of γ_{int} with respect to its *ab initio* value for the cases of a non-slipping (rigid) and a slipping interface, with and without the edge component taken into account. The number in parenthesis indicates the percentage dislocation content on the interface for the case of slipping interface with the edge component taken into account. As expected, the critical transmission stress is independent of γ_{int} for the case of a rigid interface, and its value is higher than the corresponding value when the edge component is neglected in the simulations. For the case of a slipping interface, i.e., when $\gamma_{int} < \gamma_{int}^{ab}$, the interface allows more dislocation content to spread from the glide plane to the interface. This in turn leads to a dramatic increase in the critical stress for transmission. For example, the critical stress is increased by a factor of three for $\gamma_{int} = 0.60\gamma_{int}^{ab}$, compared to the corresponding value at $\gamma_{int} = \gamma_{int}^{ab}$. On the other hand, when $\gamma_{int} > \gamma_{int}^{ab}$, the GSFS of the interface increases, the interfacial slipping becomes more difficult and the critical stress decreases more slowly saturating to a value of about 2.8 GPa. Thus, these results clearly demonstrate that the increase of transmission stress is directly related to the spreading process on the interface. Note, that the percentage of dislocation content on the interface increases from about 10% for $\gamma_{int} = 1.5\gamma_{int}^{ab}$ to 98% when $\gamma_{int} = 0.60\gamma_{int}^{ab}$. A similar trend of the critical transmission stress as a function of the interfacial energy barrier is also found for the case of slipping interface without taking into account the edge components (plain circles), but with higher values of critical stress. Our calculations show for the first time that the removal of the edge components results in dramatically different values for the transmission stress compared to those if the dissociation is included.

4. CONCLUSIONS

In conclusion, we have presented an improved coupling scheme for the original multiscale modeling approach of Choly et al. which concurrently couples DFT-based quantum mechanical calculations with empirical EAM simulations for metals. Within this scheme, the force on the DFT/EAM boundary atoms is determined from the EAM *bulk* calculations rather than from the combined DFT/EAM *cluster* calculations proposed in the original approach. In this way, the fictitious surface effects on the inner DFT atoms have been largely removed. The improved scheme reduces the coupling errors on the boundary DFT atoms and the EAM atoms by more than one order of magnitude for bulk Al, compared with the original approach. We have applied the improved method to study the core properties of an edge dislocation in Al

REVIEW

and have demonstrated that this approach yields a core structure and σ_P for Ta in excellent agreement with the FP-GFBC method.[37] We show that the *local environment* of W solutes in bcc Ta has a dramatic effect on both the dislocation mobility and slip paths: Isolated W solutes enhance the dislocation mobility, W nanoclusters of triangular shape pin the dislocation, while those of hexagonal shape result in spontaneous dislocation glide. Thus, the local chemistry plays a key role on the energy landscape of the PPS.

Using an *ab initio*-based approach of Suzuki's inter row potential, we find that Cu clusters change dramatically the core structure of a screw dislocation from non-polarized in pure Fe to polarized. These results are corroborated by atomistic simulations indicating that Cu facilitates the core planarity and enhances substantially the edge component. The core path under pure glide shear stress exhibits a *stable → metastable → stable* transition. The Peierls stress for pure Fe lies between the upper and lower values of the critical stress for the Cu precipitate. In sharp contrast, Cr solute clusters, do not change the core polarization and increase σ_P, thus hardening Fe. The underlying atomic origin responsible for the unusual lubricant effect of Cu lies on the reduction of the Fe–Cu and Cu–Cu AR interactions which are dominated by the weak t_{2g}-s hybridization. On the other hand, the Fe–Cr and Cr–Cr AR interactions are dominated by the much stronger t_{2g}–t_{2g} hybridization.

Using four different interaction models (the PDD, rigid PDD, PDD with GPN, and rigid PDD with GPN), we find that the influence of dislocation line flexibility is negligibly small, whereas the dislocation core structure has a major role in determining the CRSS. An analytical equation for coherency strengthening was revised to incorporate the dislocation core information into the evaluation of the CRSS, reproducing very well the results of detailed PDD simulations with the GPN model. The influence of the dislocation line flexibility on the stacking-fault strengthening was found to be negligible. Finally, an analytical equation, which was derived with a dislocation model composed of two partial dislocations and a stacking-fault in-between, precisely reproduced the CRSS of the stacking-fault strengthening mechanism.

Finally, we have developed a hybrid approach to study the dislocation transmission/spreading in both coherent and semi-coherent Cu/Ni bimaterial. This approach combines the parametric dislocation dynamics based of the PN framework with *ab initio*-determined GSFS. The model takes into account all three components of atomic displacements of the dislocation and utilizes the entire GSFS to reveal outstanding features of dislocation dissociation. The effects of the mismatch in the elastic properties, gamma surfaces, and misfit dislocations on the spreading of the dislocation at the interface and on the transmission across the interface are accounted for. We are able to reproduce several MD simulations trends and make further predictions

about the strength of Cu/Ni laminates, without the reliance on empirical potentials. Our calculations show that the dislocation dissociates into partials in both Cu and Ni. The dislocation core is squeezed near the interface facilitating the spreading process, and leaving an interfacial ledge during the transmission process. The dependence of the critical transmission stress on the dislocation spreading/transmission is examined. The competition of dislocation spreading and transmission depends on the GSFS of the interface. It is found that the decrease of the interfacial GSFS enhances core spreading which in turn increases the transmission stress. Moreover, it is found that the strength the bimaterial can be significantly enhanced by the presence of pre-existing misfit dislocations. In contrast to other available PN models, it is shown that the presence of all three atomic displacements of dislocation has significant effect of the transmission stress.

References

1. A. Bourret, J. Desseaux, and A. Renaul, *J. Microsc. Spectrosc. Electron* 2, 467 (**1977**).
2. Y. Takai, H. Hashimoto, and E. Endo, *Acta Crystallogr. Sect. A* 39, 516 (**1983**).
3. H.-J. Kaufmann, A. Luft, and D. Schulze, *Cryst. Res. Technol.* 19, 357 (**1984**).
4. T. Imura, K. Noda, H. Matsui, H. Saka, and H. Kimura, Dislocations in Solids, University of Tokyo Press (**1985**), p. 287.
5. N. Kioussis, M. Herbranson, E. Collins, and M. E. Eberhart, *Phys. Rev. Lett.* 88, 125501 (**2002**).
6. M. S. Duesbery, Dislocations in Solids, edited by F. R. N. Nabarro, North Holland, Amsterdam (**1989**), p. 67.
7. J. W. Christian, *Metall. Trans. A* 14, 1237 (**1983**).
8. E. Pink and R. J. Arsenault, *Prog. Mater. Sci.* 24, 1 (**1979**).
9. Y. F. Gu, H. Harada, and Y. Ro, *J. Metals* 56, 28 (**2004**).

10. T. Harry and D. J. Bacon, *Act Mater.* 50, 195 (**2002**).
11. D. R. Trinkle and C. Woodward, *Science* 310, 1665 (**2005**).
12. N. I. Medvedeva, Y. N. Grnostyrev, and A. J. Freeman, *Phys. Rev. B* 72, 134107 (**2005**).
13. A. Misra and R. Gibala, *Metall. Mater. Trans. A* 30, 991 (**1999**).
14. A. Misra, J. P. Hirth, and H. Kung, *Phil. Mag. A* 82, 2935 (**2002**).
15. D. Kramer and T. Foecke, *Phil. Mag. A* 17–18, 3375 (**2002**).
16. A. Misra, X. Zhang, D. Hammon, and R. Hoagland, *Acta Mater.* 53, 221 (**2005**).
17. E. O. Hall, *Proc. Phys. Soc.* (**1952**).
18. N. J. Petch, *J. Iron and Steel Inst.* 174, 25 (**1953**).
19. L. Fang and L. H. Friedman, *Phi. Mag.* 85, 3321 (**2005**).
20. G. Lu and E. Kaxiras, Handbook of Theoretical and Computational Nanotechnology, American Scientific Publishers, Stevenson Ranch, CA (**2005**), Vol. 22.
21. G. Lu, N. Kioussis, V. Bulatov, and E. Kaxiras, *Phys. Rev. B* 62, 3099 (**2000**).
22. S. Banerjee, N. Ghoniem, and N. Kioussis, *Second International Conference on Multiscale Materials Modeling*, edited by N. M. Ghoniem, TMS, Los Angeles, California (**2004**), pp. 23–25.
23. S. Banerjee, N. M. Ghoniem, G. Lu, and N. Kioussis, *Philos. Mag. A* 87, 4131 (**2007**).
24. E. B. Tadmor, M. Ortiz, and R. Phillips, *Philos. Mag. A* 73, 1529 (**1996**).
25. J. Gao, *Rev. Compt. Chem.* 7, 119 (**1996**).
26. J. Broughton, F. Abraham, N. Bernstein, and E. Kaxiras, *Phys. Rev. B* 60, 2391 (**1999**).
27. N. Bernstein and D. Hess, *Mat. Res. Soc. Symp. Proc.* 653, Z2.7.1 (**2001**).
28. E. Lidorikis, M. Bachlechner, R. K. Kalia, A. Nakano, P. Vashishta, and G. Z. Voyiadjis, *Phys. Rev. Lett.* 87, 086104 (**2001**).
29. V. B. Shenoy, R. Miller, E. B. Tadmor, D. Rodney, R. Phillips, and M. Ortiz, *J. Mech. Phys. Solids* 47, 611 (**1999**).
30. N. Choly, G. E. W. Lu, and E. Kaxiras, *Phys. Rev. B* 71, 094101 (**2005**).
31. L. Shilkrot, W. Curtin, and R. Miller, *J. Mech. Phys. Solids* 50, 2085 (**2002**).
32. G. Lu, E. B. Tadmor, and E. Kaxiras, *Phys. Rev. B* 73, 024108 (**2006**).
33. E. B. Tadmor, G. S. Smith, N. Bernstein, and E. Kaxiras, *Phys. Rev. B* 59, 235 (**1999**).
34. E. B. Tadmor, U. V. Waghmare, G. Smith, and E. Kaxiras, *Acta Mater.* 50, 2989 (**2002**).
35. W. E, and Z. Huang, *Phys. Rev. Lett.* 87, 135501 (**2001**).
36. R. L. Hayes, G. S. Ho, M. Ortiz, and E. A. Carter, *Acta Mater.* 86, 2343 (**2006**).
37. C. Woodward and S. I. Rao, *Phys. Rev. Lett.* 88, 216402 (**2002**).
38. Y. Liu, G. Lu, Z. Z. Chen, and N. Kioussis, *Modell. Simul. Mater. Sci. Eng.* 15, 275 (**2007**).
39. Z. Chen, G. Lu, N. Kioussis, and N. Ghoniem, *Phy. Rev. B* 77 014103 (**2008**).
40. M. S. Daw and M. I. Baskes, *Phys. Rev. B* 29, 6443 (**1984**).
41. U. Elchler, C. M. Kolmel, and J. Sauer, *J. Comput. Chem.* 18, 463 (**1996**).
42. K. W. Jacobsen, J. K. Norskov, and M. J. Puska, *Phys. Rev. B* 35, 7423 (**1987**).
43. H. Suzuki, Fundamental Aspects of Dislocation Theory, edited by J. A. Simmons, R. deWitt, and R. Bullough, National Bureau of Standards, Washington (**1970**), Vol. 4, p. 253.
44. N. M. Ghoniem, S. Tong, and L. Sun, *Phys. Rev. B* 61, 913 (**2000**).
45. M. S. Duesbery and V. Vitek, *Acta Mater.* 46, 1481 (**1998**).
46. P. E. Blöchl, *Phys. Rev. B* 50, 17953 (**1994**).
47. G. Kresse and J. Furthmüller, *Phys. Rev. B* 54, 11169 (**1996**).
48. H. J. Monkhorst and J. Pack, *Phys. Rev. B* 13, 5188 (**1976**).
49. J. P. Perdew, K. Burke, and M. Ernzerhof, *Phys. Rev. B* 77, 3865 (**1996**).
50. L. E. Shilkrot and D. J. Srolovitz, *Acta Mater.* 46, 3063 (**1998**).
51. X. Han and N. M. Ghoniem, *Phil. Mag.* 85, 1205 (**2005**).
52. A. K. Head, *Proc. Phys. Soc. LXVI* 9-B, 793 (**1952**).
53. A. K. Head, *Phil. Mag.* 7, 44 (**1953**).
54. R. G. Hoagland, T. E. Mitchell, J. P. Hirth, and H. Kung, *Phil. Mag.* 82, 643 (**2002**).
55. I. Rao and P. M. Hazzledine, *Phil. Mag. A* 80, 2011 (**2000**).
56. A. Misra, J. Hirth, and R. G. Hoagland, *Acta Mater.* 53, 4817 (**2005**).
57. G. Schoeck, *Acta Mater.* 49, 1179 (**2001**).
58. G. Schoeck, *Mater. Sci. Eng., A* 333, 290 (**2002**).
59. G. Lu, N. Kioussis, V. Bulatov, and E. Kaxiras, *Phys. Rev. B* 62, 3099 (**2000**).
60. G. Lu, V. Bulatov, and N. Kioussis, *Phys. Rev. B* 66, 144103 (**2002**).
61. G. Lu, Q. Zhang, N. Kioussis, and E. Kaxiras, *Phys. Rev. Lett.* 87, 095501 (**2001**).
62. R. Miller, R. Phillips, G. Beltz, and M. Ortiz, *J. Mech. Phys. Solids* 46, 1845 (**1998**).
63. P. M. Anderson and Z. Li, *Mater. Sci. Eng., A* 319, 182 (**2001**).
64. Y. Shen and P. M. Anderson, *TMS Letters* 1, 17 (**2004**).
65. Y. Shen and P. M. Anderson, *Acta Mater.* 54, 3941 (**2006**).
66. M. A. Shehadeh, G. Lu, S. Banerjee, N. Kioussis, and N. M. Ghoniem, *Philos. Mag. A* 87, 1523 (**2007**).
67. C. H. H. Jr. and R. G. Hoagland, *Scripta Mater.* 50, 701 (**2004**).
68. G. Fantozzi, C. Esnouf, W. Benoit, and I. G. Ritchie, *Prog. Mater. Sci.* 27, 311 (**1982**).
69. F. Nabarro, *Philos. Mag. A* 75, 703 (**1997**).
70. S. G. Srinivasan, X. Z. Liao, M. I. Baskes, R. J. McCabe, Y. H. Zhao, and Y. T. Zhu, *Phys. Rev. Lett.* 94, 125502 (**2005**).
71. J. Lauzier, J. Hillairet, A. Vieux-Champagne, and W. Benoit, *J. Phys. Condens. Matter* 1, 9273 (**1989**).
72. Q. F. Fang and R. Wang, *Phys. Rev. B* 62, 9317 (**2000**).
73. M. Mills and P. Stadelmann, *Philos. Mag. A* 60, 355 (**1989**).
74. D. L. Olmsted, K. Y. Hardikar, and R. Phillips, *Modell. Simul. Mater. Sci. Eng.* 9, 215 (**2001**).
75. M. Bujard, G. Gremaud, and W. Benoit, *J. Appl. Phys.* 62, 3173 (**1987**).
76. G. Ackland, M. I. Mendelev, D. J. Srolovitz, S. Han, and A. V. Barashev, *J. Phys.: Condens. Matter* 16, S2629 (**2004**).
77. R. Johnson, *Phys. Rev. B* 39, 12554 (**1989**).
78. V. Vitek, R. C. Perrin, and D. K. Bowen, *Phys. Rev. B* 21, 1049 (**1970**).
79. G. Wang, A. Strachan, T. Çağin, and W. A. Goddard, *Phys. Rev. B* 67, 140101 (**2003**).
80. L. Yang, P. Söderlind, and J. A. Moriarty, *Philos. Mag. A* 81, 1355 (**2001**).
81. K. Edagawa, T. Suzuki, and S. Takeuchi, *Phys. Rev. B* 55, 6180 (**1997**).
82. Z. Z. Chen, N. Kioussis, N. Ghoniem, and T. Hasebe, *Phys. Rev. B* 77, 014103 (**2008**).
83. T. Harry and D. J. Bacon, *Acta Mater.* 50, 209 (**2002**).
84. J. Marian, B. D. Wirth, R. Schaublin, G. R. Odette, and J. M. Perlado, *J. Nucl. Mater.* 323, 181 (**2003**).
85. H. Suzuki, Dislocations in Solids, edited by F. R. N. Nabarro, North Holland, Amsterdam (**1979**), Vol. 4, p. 193.
86. S. L. Frederiksen and K. W. Jacobsen, *Philos. Mag. A* 83, 365 (**2003**).
87. C. Domain and G. Monnet, *Phys. Rev. Lett.* 95, 215506 (**2005**).
88. G. J. Ackland, D. J. Bacon, A. F. Calder, and T. Harry, *Philos. Mag. A* 75, 713 (**1997**).
89. K. Tapasa, D. J. Bacon, and Y. N. Osetsky, *Modell. Simul. Mater. Sci. Eng.* 14, 1153 (**2006**).
90. V. Vitek, *Cryst. Lattice Defects* 5, 1 (**1974**).
91. S. K. Lahiri and M. E. Fine, *Metall. Trans.* 1, 1495 (**1970**).
92. V. Vitek, M. Mrovec, and J. L. Bassani, *Mater. Sci. Eng. A* 365, 31 (**2004**).

J. Comput. Theor. Nanosci. 7, 1–30, **2010**

29

REVIEW

93. J. Chaussidon, M. Fivel, and D. Rodney, *Acta Mater.* 54, 3407 (**2006**).

94. G. Simonelli, R. Pasianot, and E. Savino, *Mater. Res. Soc. Symp. Proc.* 291, 567 (**1993**).

95. P. Olsson, J. Wallenius, C. Domain, K. Nordlund, and L. Malerba, *Phys. Rev. B* 72, 214119 (**2005**).

96. D. Farkas, C. G. Schon, M. S. F. D. Lima, and H. Goldenstein, *Acta. Mater.* 44, 409 (**1996**).

97. J. Wallenius, P. Olsson, C. Lagerstedt, N. Sandberg, R. Chakarova, and V. Pontikis, *Phys. Rev. B* 69, 094103 (**2004**).

98. J. Shim, Y. Cho, S. Kwon, W. Kim, and B. Wirth, *App. Phys. Lett.* 90, 021906 (**2007**).

99. A. Caro, D. A. Crowson, and M. Caro, *Phys. Rev. Lett.* 95, 075702 (**2005**).

100. M. Y. Lavrentiev, R. Drautz, D. Nguyen-Manh, T. Klaver, and S. Dudarev, *Phys. Rev. B* 75, 014208.

101. J. H. Shim, H. J. Lee, and B. D. Wirth, *J. Nucl. Mater.* 351, 56 (**2007**).

102. N. Juslin, K. Nordlund, J. Wallenius, and L. Malerba, *Nucl. Instr. Meth.* 255, 75 (**2007**).

103. M. Miller, *Micron* 32, 757 (**2001**).

104. M. Nemoto, W. H. Tian, K. Harada, C. S. Han, and T. Sano, *Mater. Sci. Eng., A* 152, 247 (**1992**).

105. A. Takahashi and N. M. Ghoniem, *Journal of the Mechanics and Physics of Solids* 56, 15341553 (**2008**).

106. A. Takahashi, M. Kawanab, and N. M. Ghoniem, *Phil. Mag.* (**2009**), In press.

107. T. Mura, Micromechanics of Defects in Solids, Martinus Nijhoff, Dordrecht (**1982**).

108. J. D. Eshelby, *Proc. Roy. Soc. A* 241, 376 (**1957**).

109. Y. Mishin, *Acta Mater.* 52, 1451 (**2004**).

110. H. P. Karnthaler, E. T. Muhlbacher, and C. Rentenberger, *Acta Mater.* 44, 547 (**1996**).

111. A. J. Ardell, *Metall. Trans. A* 16, 2131 (**1985**).

112. V. Gerold and H. Haberkorn, *Phys. Status Solidi* 16, 675 (**1996**).

113. E. Nembach, *Scripta Mettalurgica* 20, 763 (**1986**).

114. A. Misra and H. Kung, *Adv. Eng. Mater.* 3, 217 (**2001**).

115. B. M. Clemens, K. Kumg, and S. A. Barnett, *MRS Bulletin* 24, 20 (**1999**).

116. P. M. Anderson and C. Li, *Nanostruct. Mater.* 5, 349 (**1995**).

117. J. Koehler, *Phys. Rev. B* 2, 54 (**1970**).

118. T. Foecke and D. vanHeerden, Chemistry and Physics of Nano-structures and Related Non-Equilibrium Materials, edited by E. Ma, B. Fultz, R. Shull, J. Morral, and P. Nash, TMS, Pittsburgh (**1997**), p. 193.

119. P. M. Anderson, T. Foecke, and P. M. Hazzeldine, *MRS Bulletin* 24, 27 (**1999**).

120. G. Kresse and J. Joubert, *Phys. Rev. B* 59, 1758 (**1999**).

121. G. Kresse and J. Hafner, *Phys. Rev. B* 47, 588 (**1993**).

122. N. Bernstein and E. B. Tadmor, *Phys. Rev. B* 69, 094116 (**2004**).

REVIEW